MACROPHAGE AS A DRUG DELIVERY VEHICLE FOR CANCER TREATMENT

by

WEIZHONG ZHANG

(Under the Direction of Jin Xie)

ABSTRACT

Macrophage has been recognized as an important therapeutic target owing to its multiple supportive roles in cancer development. Meantime, it has also been exploited as a potential tool for cancer treatment by taking advantage of its intrinsic properties. In the first chapter of my dissertation, I have reviewed the multiple roles of macrophage in cancer development as well as different strategies exploiting macrophages for cancer treatment. The second chapter is about using macrophage as a cellular drug delivery vehicle by making use of its tumor-tropic migration property. A drug-encapsulated silica nanocapsule is loaded into macrophages via internalization. A layer of silica shell is coated on top of the nanocapsule to prevent early leakage of drug payload during the migration towards tumor tissue. The nanocapsule-laden macrophages can efficiently home to tumor site, offering high drug delivery efficiency and enhanced therapeutic efficacy. The third chapter is about increasing the intratumoral macrophage content for enhanced tumor uptake of nanomedicine. As reviewed in the first chapter, macrophages in the tumor microenvironment can not only accumulate nanoparticles by phagocytosis, but also remodel the tumor microvironment to render a higher leakiness for the deposition of nanoparticles into tumor tissue. In this study, increasing the intratumoral macrophage number via intratumoral injection of macrophages shows promise in increasing the tumor deposition of iron oxide nanoparticles and doxove (liposomal doxorubicin, a type of therapeutic nanomedicines) in U-87MG human glioblastoma model, therefore benefiting the tumor imaging in T_2 magnetic resonance imaging (MRI) and contributing to an improved therapeutic result. In the fourth chapter, nanoparticle-laden macrophage is exploited to enhance intratumoral immunogenic cell death (ICD) process. By taking advantage of the functional plasticity of macrophage, metal oxide nanoparticles with low cytotoxicity serve as a stimulus to promote the production of damage associated molecular pattern (DAMP) molecules of macrophage. This converts macrophage into a cellular reactor for DAMP generation, which activates the ICD process in tumor site for anti-tumor immunogenicity.

INDEX WORDS: nanoparticle, macrophage, cancer, tumor, cell-mediated drug delivery, immunogenic cell death

MACROPHAGE AS A DRUG DELIVERY VEHICLE FOR CANCER TREATMENT

by

WEIZONG ZHANG

BS, Hong Kong Polytechnic University, Hong Kong, 2013

A Dissertation Submitted to the Graduate Faculty of The University of Georgia in Partial Fulfillment of the Requirements for the Degree

DOCTOR OF PHILOSOPHY

ATHENS, GEORGIA

2019

MACROPHAGE AS A DRUG DELIVERY VEHICLE FOR CANCER TREATMENT

by

WEIZHONG ZHANG

Major Professor:	Jin Xie
Committee:	Jason Locklin
	Sergiy Minko

Electronic Version Approved:

Suzanne Barbour
Dean of the Graduate School
The University of Georgia
August 2019

TABLE OF CONTENTS

Page

APPENDICES

LIST OF TABLES

Page

LIST OF FIGURES

Page

CHAPTER 1

INTRODUCTION AND LITERATURE REVIEW: MACROPHAGE AND CANCER

Historical background

The discovery of macrophages, a specific cell population that is recognized as being capable of devouring extracellular materials (i.e., phagocytosis), can date back to the 19th century. As early as 1841, Gluge first described the presence of phagocytic cells of mesodermal origin in damaged brain tissue, likely due to the exudation of leukocytes according to his speculation[1]. Later in 1860s-1870s, the accumulation of coal dust particles in miner's lung leukocytes were described by multiple scientists, and the active "consumption" of microorganisms by white blood cells had been visualized by different scientists for the first time[2]. Since then, the protective role in host defense of cellular ingestion has been inferred, but the world was not convinced until 1880s-1890s, when Elie Metchnikoff proposed the concept of cellular immunity based on his serial discoveries on "phagocytes"[3,4]. Typically, Metchnikoff discovered that phagocytes were "programmed" to migrate to, attack, and remove the foreign materials (e.g., carmine dye crystal, yeast) or degenerating cells. In 1887, the tissue-resident phagocyte populations were categorized and officially christened as "macrophage" by Metchnikoff to be distinguished from the circulating type (i.e., neutrophil). It took another hundred years to understand the functions of innate and adaptive immune systems, which collaborate with each other in host defense, as well as the role of macrophage as an innate immune cell[3]. In addition, the modern concept of the tumor microenvironment has been introduced in 1970s. Since then, the ability of macrophages in supporting tumor growth and recovery from different therapies has been spotlighted[5].

Development and functional heterogeneity of macrophage

Macrophages, which are widely present in all tissues, are derived from two sources[6–8]. The initial source refers to embryonic progenitor cells, which seed and differentiate into tissue macrophages before birth, such as Kupffer cells in liver, microglial cells of the central nerve system, etc. These residing macrophages usually reserve the long-term proliferation ability to maintain the pool. The other source arises from monocytes, which originate from bone marrow progenitors, enter bloodstream as promonocytes, develop into the mature type, extravasate into tissues in response to the chemotactic cues, and differentiate into specific types of tissue macrophages according to the microenvironment stimuli. Examples include mammary gland macrophages, intestinal lamina propria macrophages, etc.

Macrophages exhibit different functions in tissue homeostasis, host defense, and immune response regulation[9,10]. The major role of macrophage is to clear and remove the “effete”, “damaged” self (e.g., old erythrocytes, apoptotic cells, cell debris) and the extraneous materials in the interstitial -environment as a janitorial cell[9]. Meantime, macrophages serve as the primary sensor of exogenous (e.g., microorganisms) and endogenous danger signals (e.g., necrotic cell debris) through pattern-recognition receptors for innate and adaptive immune response initiation[11–13]. Furthermore, in response to cues present in different tissue microenvironments, macrophages can be polarized to distinct phenotypes with different, preferential functions, such as bone remodeling by osteoclasts, lipid buffering by adipose tissue macrophages, phagocytosis and immune surveillance by alveolar macrophages, etc.[7,8,14]. Based on the functional properties, Mosser and Edwards have tried to categorize macrophages into three different classes, including the classically activated macrophages with enhanced pro-inflammatory ability, wound-healing type macrophages primed mainly by interleukin-4 (IL-4), and regulatory macrophages with immune suppressive function[9]. To emulate the helper T cell classification (i.e., T_H1/T_H2), macrophages are still more often classified into M1 or M2 types: M1 type refers to the classically activated class, while M2 more refers to the regulatory class with or without certain levels of wound-healing function[15] (**Figure 1.1**).

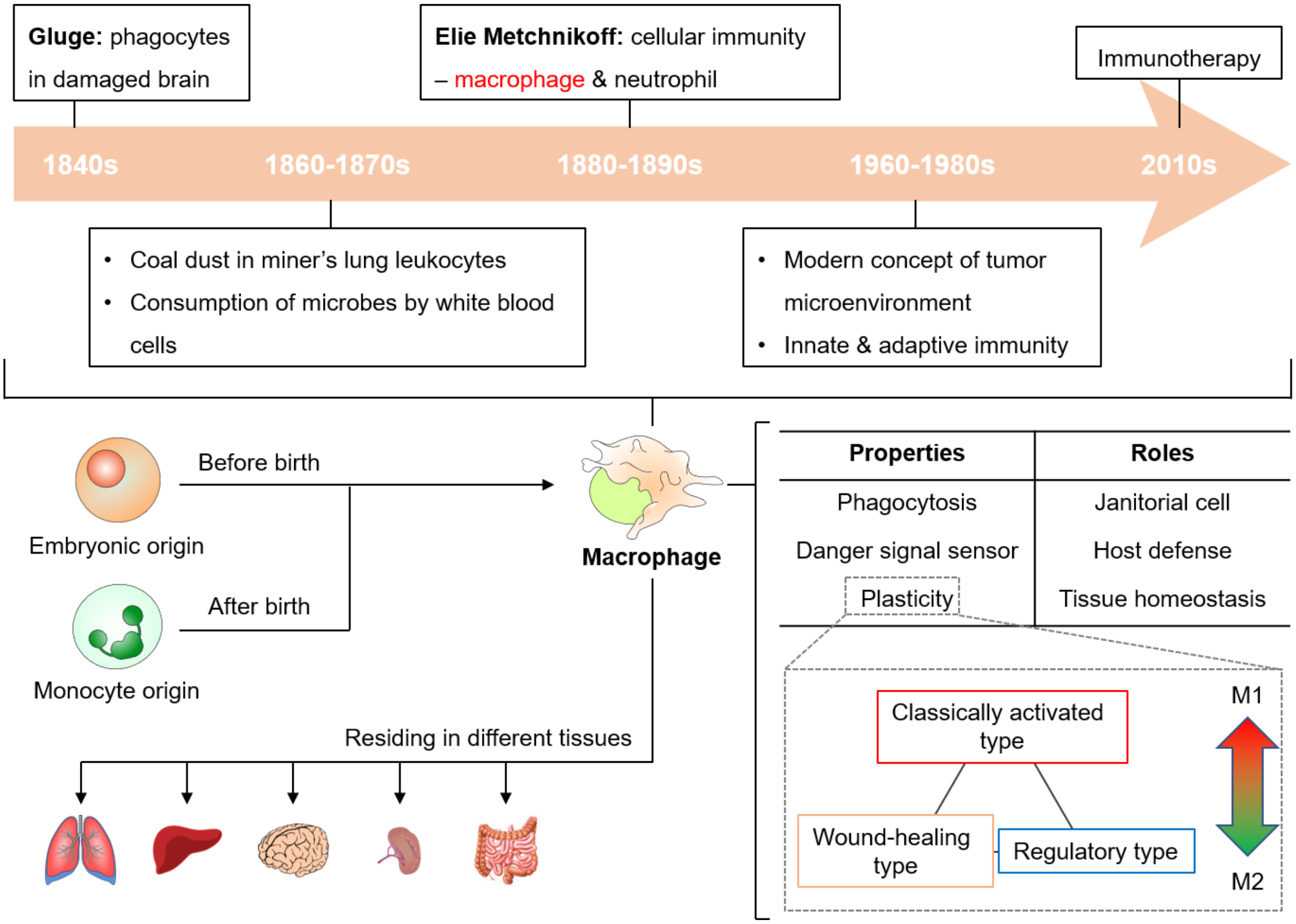

Figure 1.1. A brief introduction of macrophage about its historical background and properties.

The roles of macrophage in cancer

As one type of leukocytes widely present in various types of tumor tissues, the crucial, multiple roles of macrophages in cancer progression have not been discovered until 1990s[5,16,17]. Since then, scientists started to find that the cancer progression process is correlated with a gradual switching on the infiltrated macrophages from the classically activated types to the regulatory types with high expressions of colony-stimulating factor 1 (CSF1)[9]. As the cancer stages and grades increase, the intratumoral density of infiltrated macrophages was found mounting up significantly, while the overall ratio between the tumoricidal, M1 macrophages and the tumorigenic, M2 subsets (i.e., M1/M2 ratio) drops significantly[18]. Currently, the M1/M2 ratio is found positively correlated with and, thus, serves as a good predictor of patient survival and prognosis in different tumor models[16,19,20]. The specific roles of macrophages in different cancer stages are summarized below (**Figure 1.2**).

Tumor initiation stages

During the earliest stages, macrophages contribute to predisposing host cells to neoplastic transformation in the following three aspects. First, infiltrated M1 macrophages can produce free radicals and other mediators [e.g., reactive oxygen species (ROS), IL-6, tumor necrosis factor (TNF), interferon (IFN)-γ, etc.] to harness the inflammation, causing DNA damages and mutations in epithelial cells[5,9]. Second, the intercellular crosstalk between macrophages and epithelial cells via secreted soluble mediators contributes to nuclear factor (NF)-κB signaling activation[21,22]. Third, macrophages are found more fusogenic than other leukocytes[23], and they can actively migrate to the epithelial compartment for efficient fusion with the host cells, leading to massive chromosomal rearrangement and generation of daughter cells with novel transcriptome features[24].

Tumor progression stages

During tumor progression stages, macrophages that are recruited to the tumor mass are initially educated to become tumorigenic, M2 subsets by the stimuli present in the tumor microenvironment, including interleukin (IL)-4, 5, 10, 13, transforming growth factor (TGF)-β, glucocorticoids, prostaglandin E_2 (PGE_2), extracellular matrix components, immune complexes, apoptotic cells, necrotic cell debris, low pH, and hypoxia[16,25].

The reprogrammed macrophages function in multiple ways to benefit tumor growth. Specifically, the M2 macrophages can directly stimulate tumor proliferation with secreted soluble substances (e.g., TGF-β1, epidermal growth factor (EGF), platelet-derived growth factor (PDGF), hepatocyte growth factor, basic fibroblast growth factor (bFGF), etc.)[17,26]. Also, macrophages, which are lured and trapped in the hypoxic or necrotic areas, can indirectly support tumor growth by stimulating tumor angiogenesis with secreted cytokines and growth factors (e.g., vascular endothelial growth factor (VEGF)-A, bFGF, IL-8) and expressed enzymes (e.g. matrix metalloproteinases (MMPs), cyclooxygenase-2 (COX-2))[17].

Tumorigenic macrophages also mediate tumors circumvent immune surveillance by different means. The primary change is the down-regulation of many markers of classical activation, such as the expression of major histocompatibility complex (MHC)-I/II, nitric oxide synthase (iNOS), and the secretion of TNF-α, IL-12)[17,27]. Instead, macrophages produce large amounts of anti-inflammatory substances (e.g., IL-10, PGE_2) and overexpress inhibitory T-cell checkpoint regulators (e.g., programed cell death ligand-1/2 (PD-L1/2)) to suppress the anti-tumor immunity[16,19,28]. Meantime, the arginase activity (i.e., Arg1) is also up-regulated, which not only contributes to the formation of stroma that may prevent interaction between cytotoxic T cells and tumor cells, but also exhausts T cells by consuming Arginine[16,29,30]. Furthermore, macrophages also secret different kinds of chemoattractants (e.g., C-C motif chemokine ligand (CCL)-20, 22, etc.) to recruit other immunosuppressive cells like immature dendritic cells, myeloid-derived suppressor cells (MDSCs), and regulatory T (T_{reg}) cells[16]. Finally, the highly expressed MMP-7 protein by macrophages in the tumor hypoxic regions can cleave the Fas ligand from neighboring tumor cells, making them less sensitive to lysis by natural killer (NK) cells and cytotoxic T cells as well as some chemotherapeutic drugs[17].

Tumor metastasis

The interplay between macrophages and tumor cells has been validated as a crucial factor for lung metastasis[21,31]. One primary reason is that macrophages mediate the epithelial-mesenchymal transition (EMT) of tumor cells, in which tumor cells lose cell-cell adhesion by down-regulating E-cadherin and β-catenin and gain enhanced invasive and metastatic ability with an up-regulation of mesenchymal markers, such as N-cadherin[32]. Activated macrophages can secret soluble mediators that up-regulate genes involved in stem cell maintenance and EMT in tumor cells (e.g., CXCL3, SPP1, Sox-2, etc.) as well as EMT markers (e.g., oncostatin M)[16,26]. Meantime, macrophages help induce the activation of NF-κB, initiate and maintain EMT of tumor cells/tumor stem cells via juxtacrine signaling through cluster of differentiation protein 90 (CD90) and Eph4A receptors[16,33]. Moreover, heterotypic cell fusion between macrophages and tumor cells generates a large pool for the screening and selection of stem cell-like daughter cells with properties for metastasis (e.g., high motility, survival in circulation, tissue invasion, and growth in new sites)[24,32].

In addition, macrophages not only stimulate the formation of blood and lymphatic vessels by releasing VEGF-A and C, but also secret chemotactic signals which promote the migration and intravasation of tumor cells into the blood and lymphatic vasculature[17,34,35]. Also, macrophages help degrade the extracellular matrix by producing proteases and inhibitors (e.g., MMP-2, MMP-9) to facilitate tumor cell invasion[27].

The survival of metastatic tumor cells also significantly depends on the functional macrophages. Upon successful seeding in lung, for instance, tumor cells start to recruit metastasis-associated macrophages by different means, including endothelin-1 (ET-1) receptor pathway, CCL2-CCR2 axis, formation of clot, etc.[31] The infiltrated macrophages can further foster the tumor cell growth via CCL3 signaling or by expressing 5-lipoxygenase, for instance, and help recruit and retain circulating tumor cells at the metastatic site with α4 integrin[16,31]. Some transcriptional factors within functional macrophages are found playing crucial roles in supporting tumor metastasis, such as ETS2 and E2F3, but the mechanisms behind remain elusive[31].

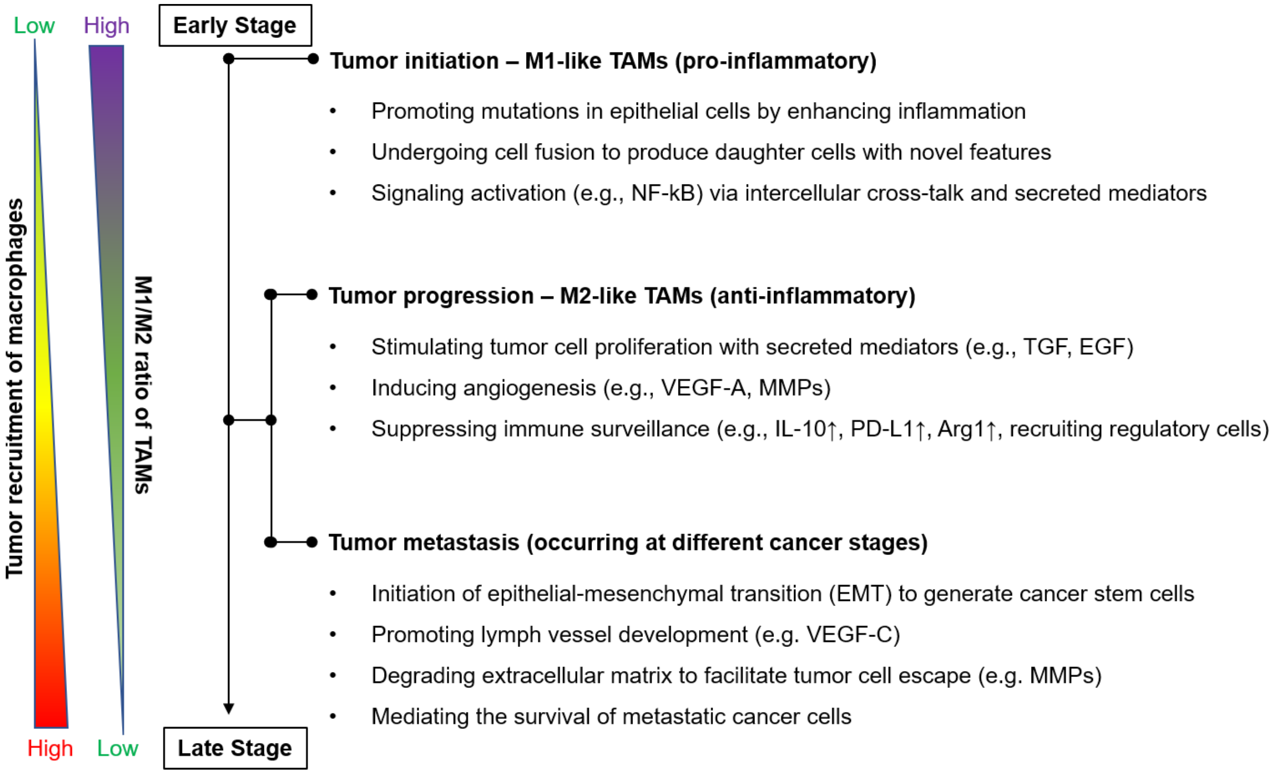

Tumor initiation – M1-like TAMs (pro-inflammatory)

- Promoting mutations in epithelial cells by enhancing inflammation
- Undergoing cell fusion to produce daughter cells with novel features
- Signaling activation (e.g., NF-kB) via intercellular cross-talk and secreted mediators

Tumor progression – M2-like TAMs (anti-inflammatory)

- Stimulating tumor cell proliferation with secreted mediators (e.g., TGF, EGF)
- Inducing angiogenesis (e.g., VEGF-A, MMPs)
- Suppressing immune surveillance (e.g., IL-10↑, PD-L1↑, Arg1↑, recruiting regulatory cells)

Tumor metastasis (occurring at different cancer stages)

- Initiation of epithelial-mesenchymal transition (EMT) to generate cancer stem cells
- Promoting lymph vessel development (e.g. VEGF-C)
- Degrading extracellular matrix to facilitate tumor cell escape (e.g. MMPs)
- Mediating the survival of metastatic cancer cells

Figure 1.2. A summary of distinct roles of macrophages in different cancer stages.

Macrophage as a therapeutic target and tool for cancer treatment

Macrophage depletion

In regard of the critical roles of tumor associated macrophages (TAMs) in cancer development, TAM depletion becomes one reasonable, straightforward method. Strategies include inhibition of CSF1-CSF1 receptor (CSF1R) axis, a key axis regulating macrophage proliferation and survival, using antibodies (e.g., RG7155, IMC-CS4, etc.) or small molecules (e.g., pexidartinib, PLX7486, etc.), and drugs that specifically induce apoptosis of macrophages, such as bisphosphonates (e.g. clodronate, zoledronic acid, etc.) and trabectedin[5,16,36,37]. Meantime, by taking advantage of the phagocytic activities of macrophages, nanoparticles laden with bisphosphonates have been developed for TAM depletion in different preclinical models, such as liposomal clodronate (i.e., clodrolip) for melanoma, folate-decorated liposomal zoledronic acid for colon adenocarcinoma, and aldendronate-glucomannan bioconjugates for sarcoma[37]. An alternative approach is to inhibit the recruitment of macrophages into tumor mass by targeting CCL2-CCR2 axis (e.g., carlumab, an anti-CCL2 monoclonal antibody, and PF-04136309, a CCR2 inhibitor), but the result is disappointing with poor prognosis owing to the compensatory proliferation of tissue-resident macrophages and the activation of certain feedback mechanism to restore the serum CCL2 level by the system post treatment[5,31].

Macrophage re-programing

Re-polarization of macrophages from the tumorigenic, M2-like phenotype to the tumoricidal, M1-like phenotype is recognized as another promising strategy to convert TAMs from an accomplice supporting tumor development to a therapeutic tool for curing cancer. Scientists have found that treatments like anti-PD-1 therapy and inhalation of aerosolized IFN-γ can efficiently drive the reversion from M2 to M1 phenotype, and the therapeutic efficacy is also largely attributed to the activation of tumor M1 macrophages with enhanced anti-proliferative activities as well as increased macrophage infiltration into the metastatic sites[31,38]. Exposure to low molecular weight hyaluronic acid (≤ 60 kDa) was also observed to induce a classically activation of macrophages by up-regulation of genes related to pro-inflammation[39,40].

Toll-like receptor (TLR) agonists represent one class of immunotherapeutic agents capable of macrophage reprograming[5]. Activation of TLRs with, for instance, pathogen infection (e.g. malaria) or microbial patterns (e.g., lipopolysaccharide (LPS)) accounts for the initiation of the macrophage-mediated programmed cell removal of cancer cells as well as innate and adaptive anti-tumor immune responses[19,41–43]. Three small molecular TLR agonists have demonstrated antitumoral properties in clinical trials, including imiquimod and 852A as TLR7 agonists and IMO-2055 as TLR9 agonist[5]. In addition, delivery of microbe-derived components to macrophages using liposomes shows promise in macrophage re-education via TLR signaling[31].

Another strategy is to treat the key signaling pathways or marker expressions that are associated with M2-like phenotype as the therapeutic targets. Intervention on these targets has shown promising therapeutic results (**Table 1.1.**). For instance, inhibition of CD40-CD40 ligand (CD40L)[5], Class IIa HDACs[44], PI3Kγ[45], Arg1[30], IκB kinase (IκKB)[46], IκBα[47], and RNase-III enzyme DICER[48], led to macrophage reprograming and switched the anti-tumor activities on. In addition, neutralization of the pattern scavenger receptor, macrophage receptor with collagenous structure (MARCO), on M2 macrophages with antibodies also repolarized TAMs to a pro-inflammatory phenotype and enhanced the tumor immunogenicity on breast, colon carcinoma, and melanoma models[49]. In another study on an allograft hepatoma murine model, CpG oligonucleotide (ODN), a pathogen-associated molecular pattern, together with anti-IL-10/IL-10R ODNs were specific-delivered to TAMs with a galactose-type lectin I decorated nanocarrier, which also boosted the anti-proliferative ability of TAMs[50].

With the progression of nanotechnology in recent years, many types of nanoparticles have also been found capable of inducing pro-inflammatory responses in macrophages owing to their intrinsic properties[51]. One canonical example is ferumoxytol, an FDA-approved iron oxide nanoparticle formulation for anemia and iron deficiency treatment, which could inhibit the growth of early adenocarcinoma and lung cancer metastases in liver and lungs in mice by switching on the pro-inflammatory Th1-type response on macrophages[52]. Another example is a glycocalyx-mimicking nanoparticle prepared via self-assembly of three sugars: galacopyranoside

(Gal), mannopyranoside (Man), and fucopyranoside (Fuc)[53]. Post internalization of nanoparticles by M2 macrophages via Man-CD206 interaction, macrophages were observed to be repolarized to M1 phenotype with upregulated CD86 expression and downregulated CD206 and CD25 expressions, and Fuc was considered playing an important role in triggering this shift. M2 macrophages can also be reprogramed by single-wall carbon nanotubes (SWCNTs), which could mimic pathogen and interact with TLR2 and TLR4 on TAMs via hydrophobic interaction[54], as well as polystyrene nanoparticles with carboxyl or amino groups on the surface[55].

As one key regulator species in macrophage signaling, ROS production plays different roles in macrophage phenotype polarization[56]. On one hand, superoxide (O_2^-) production is required for the late-phase biphasic ERK activation and differentiation into M2-phenotype macrophages, and elimination of ROS with butylated hydroxyanisole (BHA) or ROS inhibitors can efficiently block the occurrence of M2 TAMs and suppress tumorigenesis in mouse cancer models[57]. On the other hand, ROS can facilitate an M1 phenotype differentiation by serving as a 2nd messenger in regulating the downstream pathways (e.g., mitogen-activated proteinkinase (MAPK), NF-κB) and enhancing the antigen presentation function by deactivating proteases in lysosomal lumen and maintain the pH around 7.5 by consuming the protons as well as inhibiting V-H^+ ATPase[56,58,59]. In a recent study by Shi *et al.*, photogenerated ROS was exploited to repolarize macrophages to the M1 phenotype using nanoparticle-mediated photodynamic therapy[60]. Specifically, by tailored-designing two nanoparticle formulations, photosensitizer molecules were specific-delivered to the lysosomal lumen and cytoplasm of macrophages separately, allowing the generation of ROS in lysosomes and cytoplasm respectively. The results showed that ROS production in cytoplasm induced a more rapid repolarization than ROS production in lysosome. Co-delivery of a tumor-associated antigen together with ROS photogeneration induced effective immunogenicity. One interesting finding out of this study is that the lysosome-targeted group induced increased CD4$^+$ effector cytotoxic T lymphocytes, while the cytoplasm-oriented group induced more CD8$^+$ effector cytotoxic T lymphocytes. Overall, the produced ROS and the resulting cell stress may synergize with each other in the induction of macrophage phenotype repolarization.

Table 1.1. Strategies of targeting M2-like phenotype related pathways or markers

Target	Tumor Model or Cell Line	Treatment	Ref.
CD40-CD40L	clinical trials	inhibition with antibodies: CP-870,893 and RO7009789	[5]
Class IIa HDACs	luminal B-type breast cancer	inhibition with TMP195	[44]
PI3Kγ	subcutaneous LLC lung cancer, MEER & SCCVII HNSCC murine models, and orthotopic PyMT breast murine model	inhibition with TG100-115	[45]
Arg1	MC38 colon carcinoma, EL-4 lymphoma, and B16F10 melanoma murine models	inhibition with 2-*S*-amino-6-boronohexanoic acid (ABH)	[30]
IκKB	ovarian cancer model	inhibition with adenovirus infection	[46]
IκBα	ID8 murine ovarian tumor cells, wild-type bone-marrow-derived macrophages	inhibition with small interfering RNA (siRNA), delivered with mannosylated polymeric nanoparticles	[47]
Rnase-III enzyme DICER	bone-marrow-derived macrophages, transgenic and orthotopic MMTV-PyMT tumor model, subcutaneous tumor models (LLC, MC38, MC38-OVA)	*Dicer1* gene knockdown	[48]

MARCO	breast, colon carcinoma, and melanoma models	neutralization with monoclonal antibody	[49]
IL-10-IL-10R axis	allograft hepatoma murine model	inhibition of IL-10 and IL-10R with anti-IL-10 and anti-IL-10R ODNs, together with CpG ODN	[50]

TAM-mediated tumor deposition of nanoparticles

Nowadays, TAM in tumor microenvironment has been recognized as an important target of as well as a key player affecting drug delivery to tumor tissue, especially for nanoparticles[61,62]. It affects drug delivery mainly by two means. Firstly, owing to the phagocytic activity, TAM serves as the major reservoir which accumulates the majority of nanoparticle-based drug delivery vehicles and allows gradual release of therapeutic payloads to neighboring tumor cells[63–66]. Secondly, TAMs can help alter the properties of tumor microenvironment, such as tumor vessel leakiness, angiogenesis, and intratumoral pH, which allows an increased deposition of nanoparticles in the tumor interstitium and improves the tumor inhibition efficacy[67–69].

Successful drug delivery of nanoparticles to TAMs requires a minimized sequestration by the reticuloendothelial system (RES). Long circulation with neutral surface charge has been recognized as a primary requirement, which is usually achieved by surface PEGylation[65,70]. In another study by Qie *et al.*, instead of using PEG coating which reduces uptake of both M1 and M2 macrophages, CD47 coating preferentially lower the phagocytosis by M1 macrophages, which is beneficial for delivery to M2 TAMs[71]. An alternative strategy is to tailored-design nanoparticles with a flat or negative curved surface structure, such as nanoring, to minimize the uptake by RES phagocytes and improve the tumor deposition[72,73]. Some studies also illustrated that different types of nanoparticles were preferentially taken up by macrophages of a specific phenotype, such as polystyrene nanoparticles with carboxyl groups favoring M1 macrophages[71], and gold and silica nanoparticles favoring M2 macrophages[74,75]. This may offer some guidance in designing nanoparticles for drug delivery to tumors at different stages.

Specific-delivery of therapeutic agents to TAMs can be achieved via active targeting strategy. Functional molecules expressed on TAMs, such as Arg1, Fc receptors, folate receptor-β, and CD206, have been identified as TAM targets[5,76,77]. In addition, Cieslewicz *et al*. discovered a unique peptide sequence, M2pep, with high binding selectivity to murine M2 macrophages over other leukocytes using subtractive phage bio-panning method[78].

Increasing the macrophage infiltration into tumor tissue is a promising strategy with potential to boost the drug delivery efficiency. This has been verified in a study by Miller *et al*. using radiation therapy[79]. Ionizing radiation on tumor tissue induced tumor cell death and initiated the secretion of inflammatory cytokines, such as IL-1 and TNF[5]. This led to an enhanced recruitment of peripheral TAMs, which promoted extravasation of therapeutic nanoparticles and boosted their accumulation into tumor mass by 6 folds.

Macrophage-mediated programmed cell removal

Macrophage-mediated programmed cell removal, a process for clearance of apoptotic cells via phagocytosis, has been recognized as an important mechanism for cancer cell removal and T cell response initiation, but it is usually evaded by tumor cells via the CD47-CRT phagocytic axis they develop[80]. During cancer progression, tumor cells express higher levels of calreticulin (CRT) on the cell surface than normal cells, likely owing to the elevated cell stress, to facilitate tumor cell migration via interaction with thrombospondin (TSP)[81,82]. Cell surface CRT has been identified as one "*eat me*" signal molecule for the initiation of programmed cell removal by binding to CD91 on macrophages or bridging with complement protein C1q and mannose binding lectin (MBL)[80,83]. To evade the programmed cell removal, tumor cells upregulate the expression of the "*don't eat me*" CD47 molecule, which interacts with signal-regulatory protein α (SIRPα) on macrophages[82]. Therefore, re-activation of macrophage-mediated programmed cell removal of tumor cells has been recognized as another promising strategy for conquering cancer.

One method is to target the CD47-SIRPα axis. For instance, neutralization of the CD47 on tumor cells with antibodies (e.g., Hu5F9-G4, CC-90002) and blocking agents (e.g., TTI-621) has been tested in clinical trials[5], and CD47 inhibition therapy could synergize with TLR agonist treatment to enhance the programmed cell removal of tumor cells with the help of Bruton's tyrosine kinase (Btk)[41]. Meantime, injection of SIRPα-inhibited marrow-derived macrophages has also been observed in suppressing solid tumor growth by phagocytosis of tumor cells on NSG mice, which lack T cells, B cells, and natural killer cells while maintaining functional phagocytes[84]. In a recent study, *in situ* spray containing calcium carbonate ($CaCO_3$) nanoparticles that were pre-laden with anti-CD47 antibodies was exploited for post-surgical cancer treatment[85]. The decomposition of $CaCO_3$ nanoparticles could neutralize the acidic pH in the surgical wound and release the antibodies for CD47 inhibition, both of which promoted the phagocytosis of cancer cells by macrophages as well as trigger the downstream T cell response.

Introduction of additional CRT onto tumor cells to make the "*eat me*" signal stand out is another interesting method to break the CD47-CRT balance. In a study, a nanoparticle carrying both antibodies targeting human epidermal growth factor receptor 2 (HER2) and recombinant

CRT on the surface was exploited to specific-load CRT onto HER2^{high} E0771/E2 breast cancer cells to enhance the macrophage phagocytosis as well as activate the anti-tumor immune responses[86].

Macrophage as a drug delivery vehicle

Macrophage has been recognized as an appealing drug delivery vehicle for cancer treatment owing to its capability of being specific-navigated into tumor tissue by the cancer-related cues (e.g., CSF-1, VEGF, TNF, CCLs, etc.)[87–89]. In some studies, the cell membrane[90] or membrane proteins[91] derived from macrophages were used to decorate nanoparticles in order to borrow the unique property of macrophage for specific-drug delivery towards tumor. Meantime, exploiting living macrophages as a cellular delivery vehicle, via either attaching drug-laden nanocarriers on the cell surface or loading the nanocarriers inside cells, has been reported by many groups, including ours[92–98]. To be noticed, surface attachment with nanoparticles may affect the membrane function of macrophages by altering the membrane charge, consuming surface functionalities, and occupying the surface space, which may eventually compromise the tumor tropic drug delivery to certain degree[92]. For those with nanocarriers laden inside macrophages, the surface property of nanoparticle can affect its decomposition inside cell and the concurrent therapeutic payload release step. For instance, PEG corona can limit the cellular uptake of nanoparticles; the introduction of amino groups on the nanoparticle surface can offer a buffer zone to prevent nanoparticles from a rapid decomposition by lysosomal acidification and protease digestion[99].

Strategies discussed above are summarized in **Figure 1.3**.

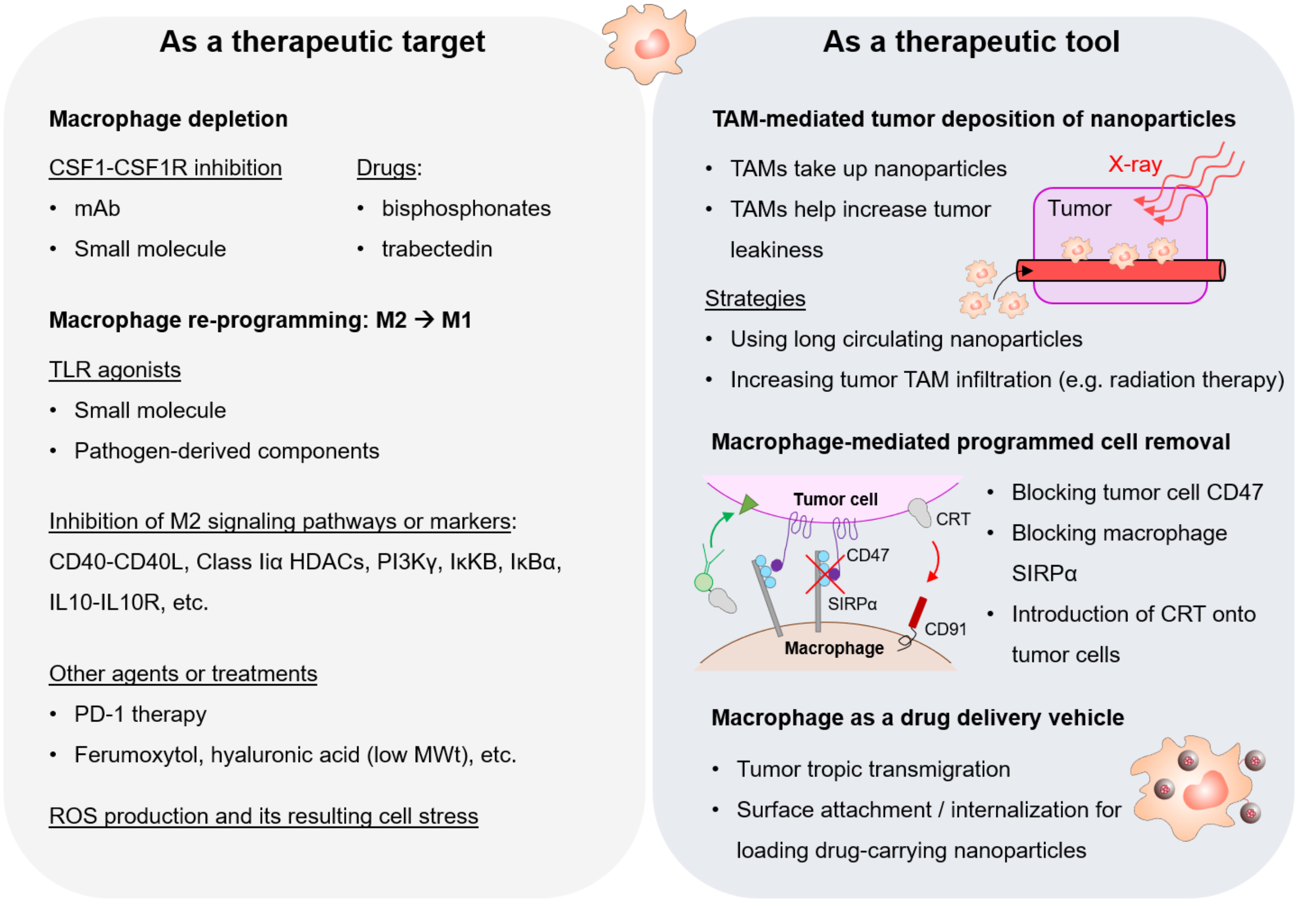

Figure 1.3. A summary of different strategies by treating macrophages as a therapeutic target and exploiting macrophages as a therapeutic tool for cancer treatment.

Future Prospective

Owing to the great plasticity and flexibility, macrophages can be polarized into distinct subsets and play different roles according to the specific microenvironment where they present. As a result, their functions vary in different cancer types, at different stages of cancer, and between primary and metastatic tumors. The tumor heterogeneity can further complex the TAM functions. In regard of this, it is necessary and judicious to make a more comprehensive profile of TAM subsets in tumors, which may benefit the cancer diagnosis and prognosis prediction.

This may require identification of distinct surface markers on TAMs, advanced tissue sampling and cell sorting techniques, more comprehensive staining, and detailed gene profiling.

Although infiltration of macrophages into solid tumors is usually associated with a poor prognosis and correlates to enhanced drug resistance in most cancer, it is still worthwhile to exploring strategies that can break the balance of intratumoral TAM content by promoting the TAM recruitment, which could not only be beneficial for drug delivery using nanoparticles but also likely show synergistic effect with other therapies (e.g., anti-PD1 therapy). It is predicted that increasing the TAM amount in solid tumors followed with macrophage re-programming treatment can significantly increase the intratumoral M1/M2 ratio, which is beneficial for cancer treatment. To achieve that, one way is to induce inflammation inside tumor tissue for TAM recruitment, such as ionizing radiation therapy, photodynamic and photothermal therapy, and microbial infection. Another strategy is to remodel the tumor microenvironment with treatments to enhance the permeability into tumor tissue (e.g., VEGF). In addition, direct administration of engineered macrophages derived in vitro represent another promising strategy. The engineered macrophages hold promise in specific-accumulating in tumor site and performing multiple tasks, including remodeling the tumor microenvironment, performing treatment, delivering drugs, and initiating T cell responses. One example is chimeric antigen receptor macrophages (i.e., CAR-M)[100].

In regard of the systemic property of cancer, the macrophages residing in other major organs may also serve as a potential therapeutic target. For instance, the inflammation status in RES organs (e.g., liver) may induce repolarization of the residing macrophage phenotype, which may affect the drug delivery efficiency using nanoparticles[74]. Also, for many organ-tropic metastasis, targeting the macrophages residing in the organs of high metastasis risk according to the cancer type and diagnosis is likely beneficial for the prognosis[31].

Overview of the following chapters

The next three chapters present three different studies about exploiting macrophages for cancer diagnosis and treatment. In the first study (Chapter 2), which was published on Advanced Materials, 2018, 1805557, 1-11, we aim to take advantage of the tumor tropic migration property of macrophages to improve the delivery efficacy of chemotherapeutic drugs to tumor mass. By tailored-designing a drug-encapsulated silica nanocapsule with slow drug release property, we loaded this nanocapsule into macrophages with a high loading yield and achieved little drug leakage during the transmigration towards tumor tissue. The nanocapsule-laden macrophages could specific-migrate to tumor in 6-24 hours post injection and release drug molecules for cancer treatment, offering an improved therapeutic efficacy without detectable side effects. In the second study (Chapter 3), we aim to investigate whether increasing the macrophage content inside tumor, via local supplementation of additional macrophages, can help improve tumor leakiness for the tumor uptake of nanoparticles. The imaging and therapy results confirm our hypothesis that the deposition of iron oxide and liposomes in tumor was boosted by macrophage supplementation. In the last study (Chapter 4), we aim to engineer macrophages into a cellular reactor for *in situ* production of damage-associated molecular pattern (DAMP) molecules to initiate the immunogenic cell death (ICD) process inside tumor for anti-tumor immunogenicity. The preliminary results indicate a positive effect of metal oxide nanoparticles promoting ATP and calreticulin production of macrophages.

CHAPTER 2

NANOPARTICLE-LADEN MACROPHAGES FOR TUMOR-TROPIC DRUG DELIVERY[1]

---

[1] Weizhong Zhang, Mengzhe Wang, Wei Tang, Ru Wen, Shiyi Zhou, Chaebin Lee, Hui Wang, Wen Jiang, Ian Michael Delahunty, Zipeng Zhen, Hongmin Chen, Matthew Chapman, Zhanhong Wu, Elizabeth W. Howerth, Houjian Cai, Zibo Li, Jin Xie. *Adv. Mater***.** 2018, 1805557, 1-11.

Reprinted here with permission of the publisher.

Abstract

Macrophages hold great potential in cancer drug delivery because they can sense chemotactic cues and home to tumors with high efficiency. However, it remains a challenge to load large amounts of therapeutics into macrophages without compromising cell functions. Here we report a silica-based drug nanocapsule approach to solve this issue. Our nanocapsule consists of a drug-silica complex filling and a solid silica sheath, and it is designed to minimally release drug molecules in the early hours of cell entry. While taken up by macrophages at high rates, the nanocapsules minimally affect cell migration in the first 6-12 h, buying time for macrophages to home to tumors and release drugs *in situ*. In particular, we show that doxorubicin (Dox) as a representative drug can be loaded into macrophages up to 16.6 pg/cell using this approach. When tested in a U87MG xenograft model, intravenously (i.v.) injected Dox-laden macrophages show comparable tumor accumulation as untreated macrophages. Therapy leads to efficient tumor growth suppression, while causing little systematic toxicity. Our study suggests a new cell platform for selective drug delivery, which can be readily extended to the treatment of other types of diseases.

Introduction

Exploiting immune cells for drug delivery is an emerging area of research.[1–3] Many types of leukocytes, including macrophages, neutrophils, and dendritic cells, can sense chemokine and cytokine cues and home to inflamed tissues. Macrophages or their predecessor monocytes in particular, can respond to cancer-related cytokines (e.g., CSF-1, VEGF, PDGF, TNF, IL-1, IL-5, etc.) and chemokines (e.g., CCL-5, 7, 8, 12, etc.),[4–6] and navigate to the diseased sites, passing multiple biological barriers along the way. This holds true for central tumor areas, which are often avascular and inaccessible to conventional therapeutics. These unique properties make macrophages a potentially appealing vehicle for cancer drug delivery.

Despite the promises, it remains a challenge to load large quantities of drugs into macrophages. Conventionally, the most common cell loading strategy is to conjugate drug molecules or tether drug-loaded nanoparticles onto the cell plasma membrane.[7] This so-called "backpack" approach has been exploited by others and us to load therapeutics onto stem cells,[8–11] leukocytes,[12–15] red blood cells,[16] and T cells[17] with varying success. However, plasma membrane is essential for cell functions and plasticity, and nanoparticle loading may adversely affect cell signal transduction, adhesion, and migration. According to Irvine et al.,[17,18] nanoparticles can occupy up to 5% of plasma membrane without significantly affecting cell functions. This translates to a drug loading rate of less than 1.0 μg per million cells (Supporting Information). Considering that in a normal cell transfer procedure 1-10 million cells are injected, the amount of drugs that can be delivered using this approach is very limited; not to mention that macrophages are phagocytes, and membrane-bound nanoparticles are often quickly engulfed by cells rather than residing on the surface.

An alternative strategy is to load drugs into the cell cytosol. This approach is considered challenging or not feasible because most chemotherapeutics are highly toxic to macrophages. Incubating macrophages with high concentrations of drugs induces immediate cell death, whilst sub-lethal dose incubation causes insufficient drug loading. There have been some successes of exploiting macrophage plasma membrane as a camouflage to improve nanoparticles' pharmacokinetics.[19,20] A few groups have attempted to load liposome or polymer nanoparticles into live macrophages,[21–23] but the difficulties to achieve high drug loading while maintaining cell functions have limited the related developments.

Herein we report a unique nanocapsule technology to solve the macrophage drug loading issue. We and others observe that it takes 6-12 h for intravenously (i.v.) injected macrophages to migrate to inflamed tissues.[6,24] We reason that if drug-loaded nanoparticles do not release the payloads in the early hours of cell entry, the adverse impacts can be held in check in spite of a high apparent drug content. This would buy time for macrophages to traffic to tumors, and release therapeutics *in situ* to induce efficient and selective cancer cell killing (**Figure 2.1**). For the purpose, it is desired that nanoparticles have a two-phase drug release profile, with minimal drug liberation in the first 6-12 h and controlled release afterwards. This is challenging because nanoparticles after internalization are trapped in the phagolysosomes of macrophages, which are rich in hydrolytic enzymes and reactive oxygen species (ROS), and can quickly digest conventional drug carriers.[25,26] To solve the issue, we created a drug-silica nanocapsule platform, consisting of a drug-silica nanocomplex core, and a solid silica sheath. The silica coating is more resistant to degradation and oxidation than alternative materials such as polymers or liposomes; by fine-tuning the coating thickness, stalled drug released would be achieved and the degree of extended release adjusted. The drug-silica nanocomplex is more susceptible to degradation than the shell as drug molecules create *de facto* defects in the silica matrix,[27] leading to two-phased drug release. Meanwhile, because drug molecules are electrostatically bound with silica, burst drug release, which is commonly seen with conventional drug carriers, should be avoided. All these properties should allow for high drug loading into macrophages while minimally affecting cell migration. We tested this hypothesis with doxorubicin (Dox) as a representative chemotherapeutic drug, and we evaluated the efficiency of drug delivery first *in vitro* and then *in vivo* in U87MG tumor bearing mice.

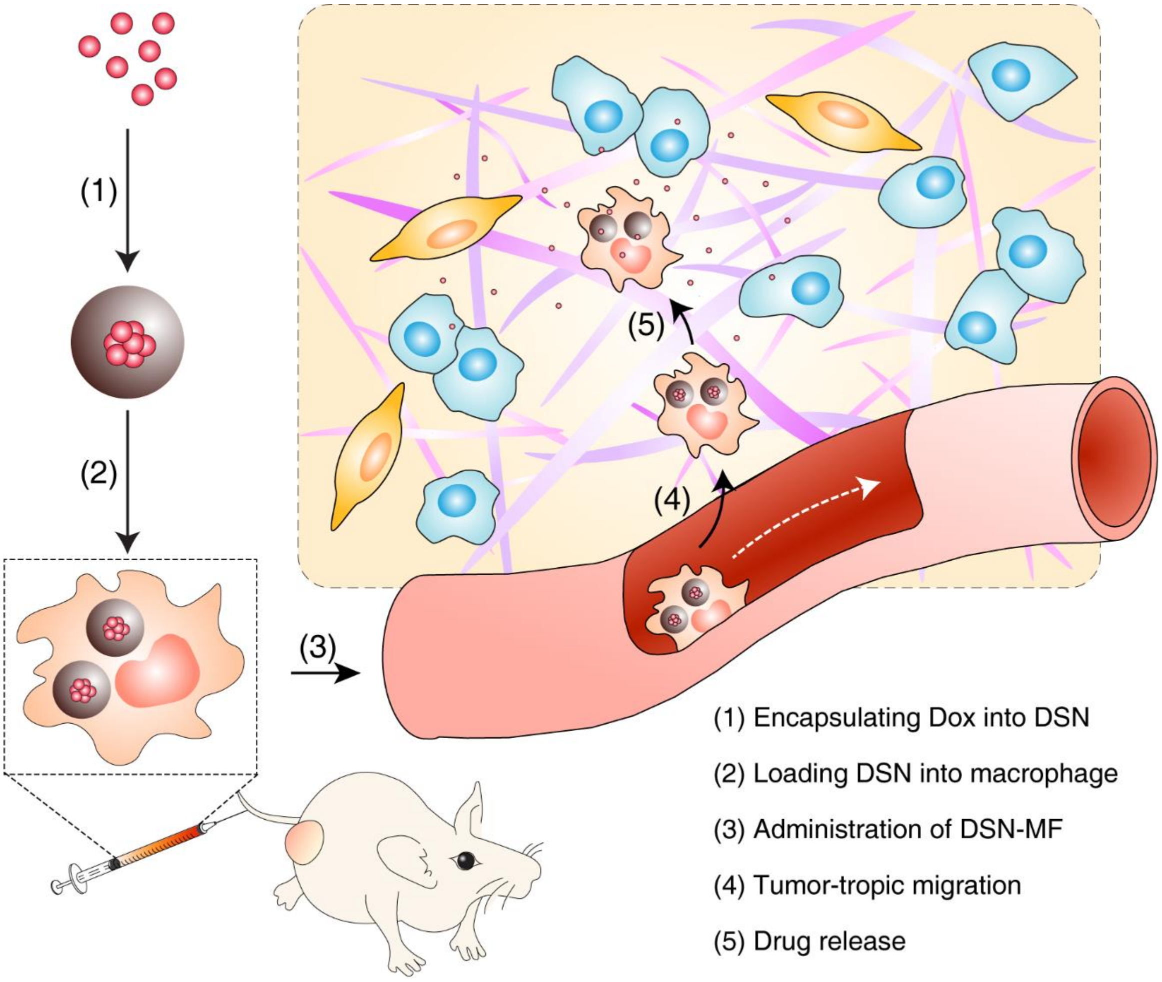

Figure 2.1. Nanocapsule-laden macrophages for drug delivery to tumors. (1) Antineoplastic drug, in this particular case Dox, was first loaded into a carefully tailored nanocapsule called drug-silica nanocomplex (DSN); (2) DSN nanoparticles were engulfed by macrophages *ex vivo*; (3) DSN-laden macrophages (DSN-MF) were i.v. injected to a tumor bearing mouse; (4) chemotactic migration of DSN-MF to tumors; (5) DSN-MF releases Dox inside tumor to selectively kill cancer cells.

Results

DSN synthesis and physical characterizations

We first synthesized Dox-silica nanocomplexes (referred to as DSN-0) by co-condensation of Dox and tetraethyl orthosilicate (TEOS, Dox: TEOS molar ratio of 1:13) in ethanol. Dox is positively charged at this condition and electrostatically bound with TEOS, whilst being intercalated into the growing silica matrix.[27] The resulting DSN-0 nanoparticles were 28.4 ± 3.4 nm in diameter (**Figure 2.2a**). They were stably dispersed in PBS (**Figure S1b, S1c**), with a slightly negatively charged surface (-6.9 ± 1.0 mV, **Figure 2.2b**). Based on UV-Vis spectroscopic analysis, it was estimated that the Dox accounted for 16.7 wt% of the DSN-0 weight (**Table S2**).

Despite the strong electrostatic interaction, up to 11.7% of Dox was released within 12 h at pH 5.0 (close to lysosome pH;[28] **Figure 2.2c**). To minimize drug release in the early hours, we imparted a silica capsule onto the surface of DSN-0 through the Stöber method. By varying the TEOS precursor amounts, we were able to prepare DSN nanocapsules with silica coating thicknesses of 12, 22, and 52 nm (**Figure 2.2a**), and the resulting nanoparticles were referred to as DSN-12, DSN-22, and DSN-52, respectively. We found that a thicker silica coating was associated with more negative surface charge (**Figure 2.2b**) and more extended drug release (**Figure 2.2c, S1a**). Specifically, DSN-12 and DSN-22 released 10.3% and 8.0% of their Dox contents at 12 h (pH 5.0), and for DSN-52, this number was reduced to 5.1%. We also investigated DSN-52's morphology changes over time in both neutral and acidic solutions. At pH 7.4, DSN-52 remained intact for over 72 h (**Figure S1d**). At pH 5.0, on the other hand, we found no obvious morphology changes in the first 6 h, but signs of nanoparticle degradation at 24 h (**Figure 2.2d**). The gradual erosion of the silica coating then exposes the DSN core. Unlike solid silica, where adjacent silicon atom is covalently linked by an oxygen bridge, the silica matrix of DSN is more susceptible to hydrolysis due to the Dox dopants. In samples taken at later time points of incubation, we spotted many hollow capsules, suggesting the degradation of the DSN cores (**Figure 2.2d**). This correlates with faster drug release recorded after 12 h. For comparison, we also assessed drug release with Dox-loaded liposomes (i.e., Doxove) and mesoporous silica nanoparticles at the same condition. In both cases, we found significant early-hour burst release, with 26.2% (Doxove, **Figure S2a**) and 58.6% (mesoporous silica nanoparticle, **Figure S2b**) of their Dox contents liberated at 12 h, respectively.

Imparting silica coating diluted the drug content in the nanoparticles. Specifically, the Dox loading was 11.2, 8.9, and 5.1 wt%, respectively, for DSN-12, DSN-22, and DSN-52, compared to 16.7 wt% for DSN-0 (**Table S2, S3**). While it is possible to further increase the silica coating thickness and stall the drug release process, it is speculated that a too diluted drug content in the particles (e.g. less than 5%) may adversely affect Dox loading into macrophages. Due to this consideration, we selected the DSN-52 formulation for subsequent cell and animal studies.

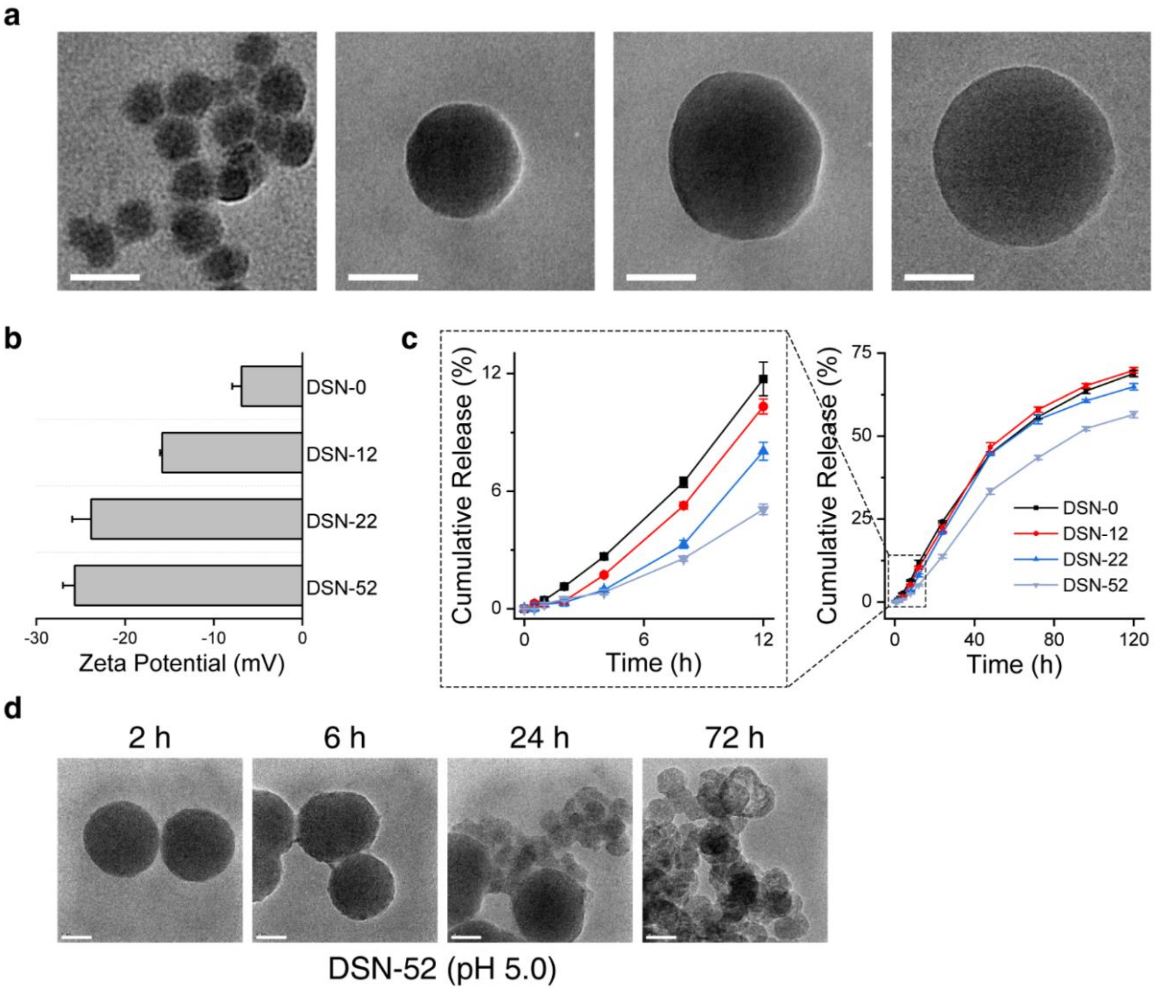

Figure 2.2. Physical characterizations of DSN nanoparticles. **a)** TEM images and **b)** zeta potential of DSN-0, DSN-12, DSN-22, and DSN-52 nanoparticles. **c)** Drug release profiles of DSN-0, DSN-12, DSN-22, and DSN-52 nanoparticles, measured at pH 5.0. **d)** TEM images of DSN-52 nanoparticles after incubating in a pH 5.0 solution for different times. Scale bars, 50 nm.

Loading DSN-52 nanocapsules into macrophages

We incubated DSN-52 with RAW264.7 cells, a murine macrophage cell line, and stopped the incubation at different times to analyze nanocapsule uptake by measuring the amount of cellular Dox on a per cell basis. We found that 2 h incubation led to efficient Dox uptake, while extending incubation further minimally increased the cellular Dox contents (**Figure 2.3a**). The uptake is attributed to macrophage phagocytosis of nanoparticles, which was observed by others with nanoparticles of comparable sizes.[22] The uptake was concentration dependent. When incubated with DSN-52 at 10, 20, and 40 μg Dox mL^{-1}, the cell Dox content at 2 h was 9.8, 15.9, and 21.3 pg cell^{-1}, respectively (**Figure 2.3b**). As a comparison, Doxove showed a Dox loading of less than 1 pg cell^{-1} at the same conditions (**Figure S4a**).

After 2 h incubation, we replenished the incubation medium and analyzed the viability of the DSN-laden cells. When initial DSN-52 concentration was 20 μg Dox mL^{-1} or below, cell viability maintained at ~70% or above at 12 h (**Figure 2.3c**). This is striking considering that the IC_{50} of free Dox is 1.5 μg mL^{-1} (**Figure 2.3d**). Based on these observations, we chose 20 μg Dox mL^{-1} and 2 h incubation for drug loading. Under this condition, macrophages bore a stunning Dox content at 16.6 ± 4.8 pg Dox cell^{-1}. Calcein AM/EthD-III assay showed that 99.2% of DSN-52 loaded macrophages (DSN-MF) were heathy at the completion of nanoparticle incubation (**Figure 2.3e**). Incubation at 4˚C in the presence of 0.1 wt.% NaN_3 led to ~80% decrease of cellular uptake, suggesting that the nanoparticle uptake was mainly mediated by endocytosis (**Figure S3**).

One concern is that the intracellular Dox, while not lethal, may affect cell functions. In particular, the nanoparticle loading may compromise cells' chemotactic migration toward cancer cells. We examined this in a transwell experiment, where U87MG glioblastoma cells were seeded onto the bottom chamber of the device, and DSN-MF loaded onto the top. We found that DSN-MF could efficiently transmigrate the well (**Figure 2.3f, 2.3g**), with both invasion and migration percentages comparable to untreated RAW264.7 cells (referred as MF onward, **Figure 2.3h, 2.3i**). Meanwhile, when U87MG cells were absent, there was no cell transmigration

(**Figure S5a**).

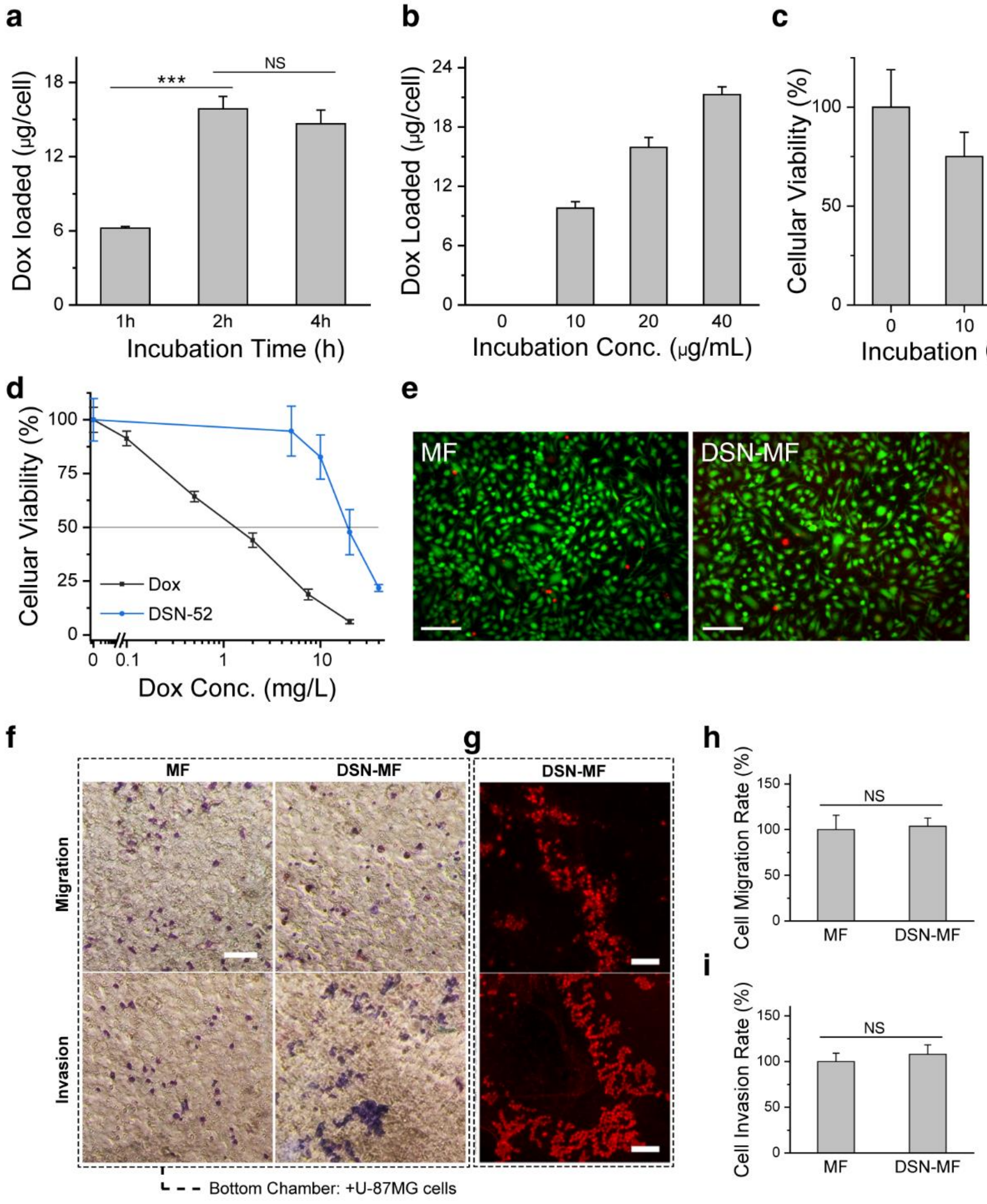

Figure 2.3. DSN-52 nanoparticles uptake by macrophages (RAW264.7 cells). **a)** Intracellular Dox contents, measured at 1, 2, and 4 hours' incubation with DSN-52 nanoparticles. ***, $p<0.001$. NS, not significant. **b)** Intracellular Dox contents, measured when the initial DSN-52 Dox concentration was 0, 10, 20, and 40 μg mL^{-1}. The incubation time was fixed at 2 h. **c)** Cell viability at 12 h via MTT assay. The cells were first incubated with DSN-52 at 0, 10, 20, and 40

μg mL^{-1} (Dox concentration) for 2 h. After PBS washing, fresh growth medium was added, and cell viability was measured at 12 h by MTT assay. **d)** Cell viability at 24 h via MTT assay. Dox (black curve), RAW264.7 cells were incubated with free Dox for 24 h. DSN-52 (blue curve), RAW264.7 cells were laden with DSN-52 and then incubated in normal growth medium for 24 h. **e)** Live and Dead cell assay results of DSN-MF and MF cells at 2 h. Green, living cells; red, dead cells. Scale bars, 100 μm. **f)** Transmigration assay. DSN-MF or MF cells were loaded onto the top of a transwell chamber, whilst U87MG cells were seeded at the bottom. Macrophages were stained into blue color via Giemsa staining. Scale bars, 100 μm. **g)** Fluorescence microscopic images of invaded/migrated DSN-MF cells, the experimental conditions were the same as those in **f**. Scale bars, 100 μm. Percentages of DSN-MF and MF cells that had **h)** migrated and **i)** invaded. NS, not significant.

We also examined the impact of DSN-52 loading on macrophage phenotype changes. Specifically, we analyzed the amounts of cytokines, including IL-1β, IL-6, IL-12, TNF-α, and IL-10, that were secreted from DSN-MF. Except for IL-1β, which showed comparable secretion relative to the control, other pro-inflammatory markers, including IL-6, IL-12 and TNF-α, all showed significantly elevated secretion (**Figure 2.4a-e**). In particular, the IL-6 level was drastically increased from 9.1 pg mL^{-1} in untreated macrophages to 484.2 pg mL^{-1} in DSN-MF at 24 h (**Figure 2.4b**). On the contrary, the level of IL-10, an anti-inflammation marker, was reduced from 8.1 pg mL^{-1} in the control to 4.8 pg mL^{-1} DSN-MF at 24 h ($p < 0.001$, **Figure 2.4c**). Accompanied with it, the IL-12/IL-10 ratio was increased from 2.2 in MF to 8.0 in DSN-MF (**Figure 2.4f**). These results indicate that RAW264.7 cells after DSN-52 loading were polarized toward the pro-inflammation M1 phenotype.[29,30]

We then analyzed Dox efflux. We observed time-dependent increase of Dox content in the supernatant of DSN-MF, which released over 50% of the loaded Dox within 48 h (**Figure 2.4g, Table S4**). We took the supernatants from different time points and added them to the incubation media of U87MG cells cultured in separate plates (**Figure 2.4a**). For the 48-h conditioned medium, incubation with U87MG led to extensive cell uptake of Dox (**Figure S5b**), which eventually led to cell death (**Figure 2.4h**). Notably, conditioned medium taken at 12 h caused little U87MG cell viability drop (**Figure 2.4h**), which is attributed to the stalled drug release of the nanocapsules.

Interestingly, Dox was not released entirely in the form of free molecules. When analyzing DSN-MF conditioned medium, we found many nanoparticles with a size of 50-150 nm in the supernatant (negative staining TEM, **Figure 2.4i**). Through a series of centrifugation (**Supplementary Information**), we were able to enrich these nanoparticles (**Figure 2.4i**). Further Western blotting analysis found high contents of Flotilin-1, TSG101, and CD81 in these nanoparticles (**Figure 2.4j**), suggesting that these were exosomes secreted by macrophages.[31] Spectroscopy analysis revealed that a 16.5% of the released Dox was entrapped within the secreted exosomes (**Figure 2.4i-j, Figure S5c, Table S4**). Considering possible exosome loss during differential centrifugation, the actual percentage of Dox released in exosomes could be even higher. Unlike artificial liposomes or micelles, exosomes present on their surface adhesion proteins, integrins, and tetraspanins, which may facilitate cancer cell uptake.[32,33] It is envisioned that during therapy, DSN-MF produces Dox-laden exosomes *in situ* inside tumors, further improving the selectivity and efficiency of the delivery approach.

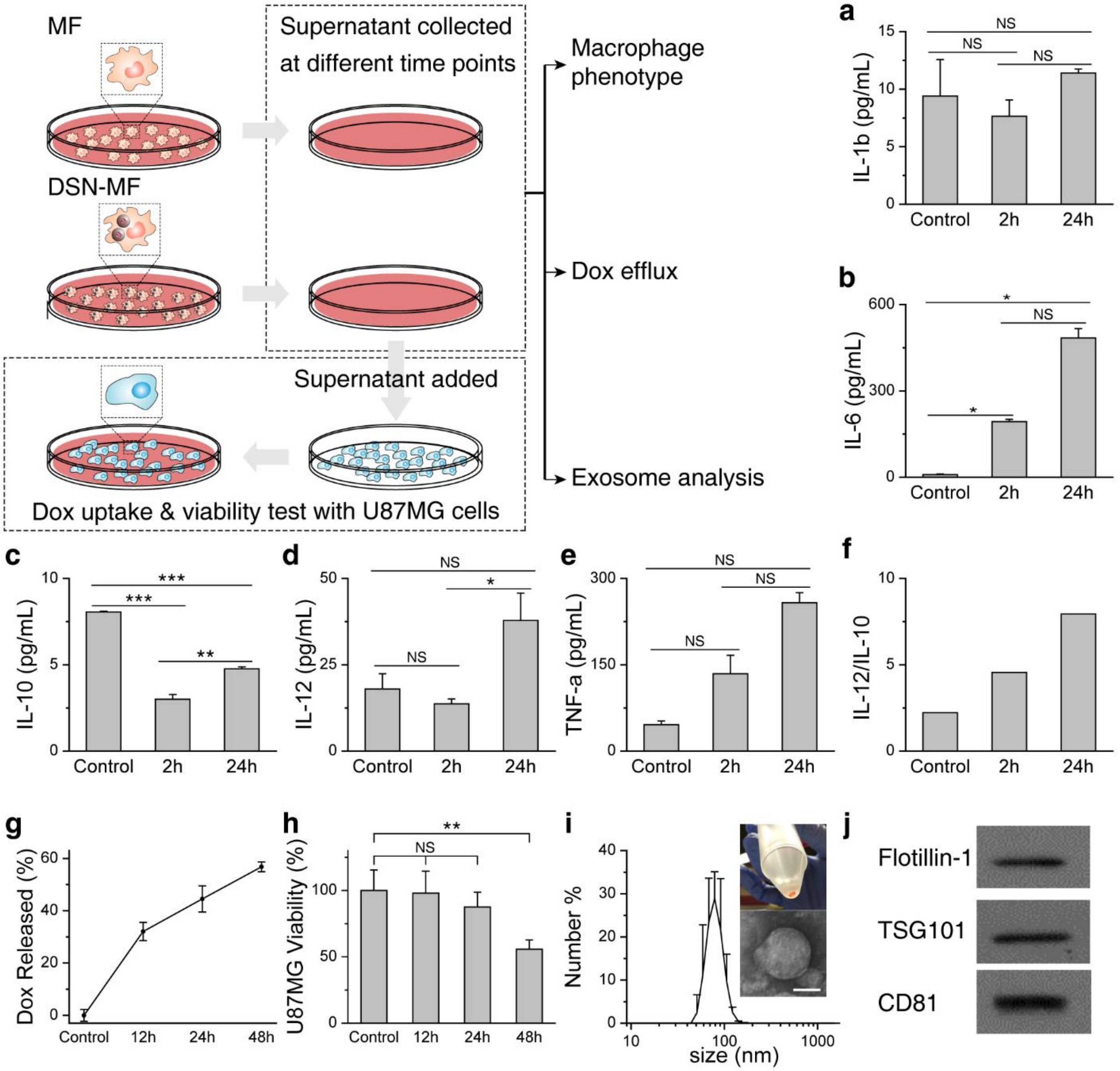

Figure 2.4. Impact of DSN loading on macrophage. Secretion of **a)** IL-1β, **b)** IL-6, **c)** IL-10, **d)** IL-12, and **e)** TNF-α from DSN-MF at 2 and 24 h. MF (untreated RAW264.7 cells) served as controls. **f)** IL-12/IL-10 ratio at 2 and 24 h. **g)** Percentage of Dox released from DSN-MF at different times (Dox retained in cell debris is excluded by centrifugation). **h)** Cell viability assay results with U87MG cells. Supernatants taken from DSN-MF culture dishes at different time points were added to a separate plate grown with U87MG cells. Cell viability was measured after 48 h incubation. *, $P<0.05$; **, $P<0.01$; ***, $P<0.001$; NS, not significant. **i)** Hydrodynamic size

of exosomes via DLS analysis (z-average size = 97.35 nm, PDI = 0.127). Exosomes were collected from DSN-MF supernatant at 48 h via centrifugations. An inset photograph of the resulting exosomes and a negative-stained TEM image were also shown. Scale bar, 50 nm. **j)** Western blot analysis of exosome lysates. Flotilin-1, TSG101, and CD81, three markers of exosomes, were detected.

In vivo bio-distribution studies

We studied the tumor tropic properties of DSN-MF in U87MG tumor bearing nude mice. To keep track of the cells, we co-loaded 50 nm iron oxide nanoparticles (IONPs)[34,35] into DSN-MF and i.v. injected 2 × 10^6 of the cells into each animal (n = 3). T_2-weighted magnetic resonance imaging (MRI) found minimal signal changes in tumors at 4 h, but extensive hypointensities at 24 h (**Figure 2.5a**). To verify cell migration, we also labeled the cell membrane with DiD, and examined the tumor samples by histopathology at 24 h post i.v. injection. We observed positive Prussian blue staining (**Figure S6**) within tumors, along with signals from Dox and DiD dye (**Figure 2.5b**), confirming that macrophages as a vehicle can deliver Dox to tumors.

For quantitative analysis, we also labeled DSN-MF and untreated RAW264.7 cells (MF) with ^{64}Cu-pyruvaldehyde-bis(N4-methylthiosemicarbazone, ^{64}Cu-PTSM) and monitored cell migration by positron emission tomography (PET).[36] We found that the majority of macrophages were initially accumulated in the lung (**Figure 2.5c**). This was attributed to the pulmonary first-pass effect, which is commonly seen with i.v. injected cells.[37,38] Specifically, the lung uptake at 1 h was 18.30 and 13.64 %ID g^{-1}, respectively, for DSN-MF and MF (**Figure**

2.5d, 2.5e). Between 1 and 8 h, there was a significant decrease of radioactivity in the lung. Meantime, tumor accumulation was significantly increased (**Figure 2.5f**), suggesting chemotactic migration of macrophages to tumors. For DSN-MF, the decay-adjusted tumor-to-liver ratio (TLR) was increased from 0.18 at 1 h, to 0.32 and 0.39, respectively, at 8 and 23 h (**Figure 2.5g**). These values were not significantly different from the MF group (p>0.05). In general, DSN-MF showed comparable pharmacokinetics to untreated macrophages (**Figure 2.5c-g**), suggesting negligible impact of DSN loading on tumor migration.

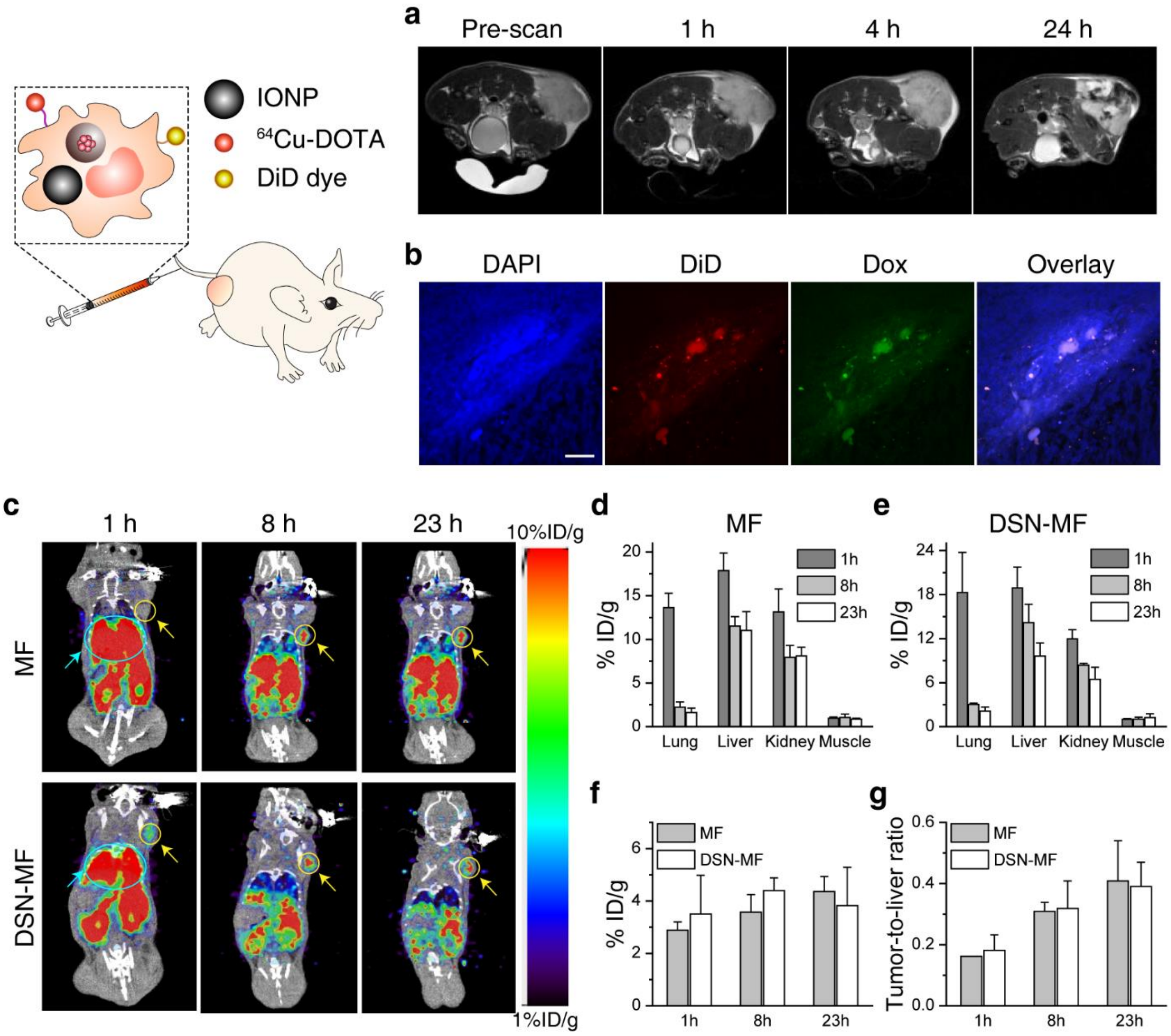

Figure 2.5. *In vivo* tumor targeting of DSN-MF, evaluated in nude mice bearing subcutaneously inoculated U87MG tumors. **a)** Axial T_2 MR images, acquired at 0, 1, 4, and 24 h post i.v. injection of DSN-MF cells. The cells were pre-loaded with iron oxide nanoparticles. **b)** Confocal microscopic images of tumor cryo-sections using the z-stack scan mode (step = 2 μm). DSN-MF cells were pre-labeled with DiD. Red, DiD; green, Dox; blue, cell nuclei. Scale bars, 50 μm. **c)** Decay-corrected whole-body coronal PET images, acquired at 1, 8, and 23 h post injection. DSN-MF or MF cells were labeled with ^{64}Cu-PTSM. Tumor area was highlighted with yellow cycles; lung area was highlighted using cyan cycle. **d, e)** Distribution of **d)** MF cells and **e)** DSN-MF cells in the lung, liver, kidney, and muscle at different time points. **f)** Tumor uptake of MF and DSN-MF cells at different times. **g)** Tumor-to-liver ratios of MF and DSN-MF cells, based on images results in **c**.

Therapy studies

The therapy study was also conducted in U87MG subcutaneous tumor models. We started therapy when the tumors reached to a size of ~100 mm^3. The animals were randomly sorted to receive the following treatments (n=5) via intravenous injection on Day 0: i) PBS; ii) free Dox (3 mg Dox kg^{-1}); iii) DSN-52 only (3 mg Dox kg^{-1}); iv) untreated RAW264.7 cells (MF, ~4 × 10^6 cells per mouse); v) DSN-MF (3 mg Dox kg^{-1}, ~4 × 10^6 cells per mouse). Only one dose was given to the animals.

For the Dox, DSN-52, and MF groups, we observed marginal tumor suppression. On Day 14, the average tumor volumes were 1328.6, 1528.47, 1442.27 mm^3, respectively, for the three control groups. Relative to the PBS group, the tumor growth inhibition (TGI) rates were 24.84%, 12.35%, and 17.73%, but the changes were insignificant (p = 0.17, 0.80, and 0.32, respectively, **Figure 2.6a**, **Figure S7a**). There was also no benefit in survival. The median survival was 16, 14, and 14 days, respectively, for the Dox, DSN-52, and MF groups, compared to that of 14 days for the PBS control (**Figure 2.6c**). As a comparison, the DSN-MF group showed an impressive TGI rate of 62.66% on Day 14, and the treatment significantly extended the animal median survival to 26 days. No body weight loss was observed during the whole treatment process (**Figure 2.6b**).

In separate studies, we euthanized mice 24 h after treatment, and performed *in situ* apoptosis staining (Abcam) on the tumor tissues (**Figure 2.6d, Figure S7b**). DSN-MF treatment led to extensive cell apoptosis. The positive staining was found at both the peripheral and central tumor areas and occupied 17.83% area of the whole tissue region, which was significantly higher than the controls (**Figure S7c**). This is again attributed to the capacity of macrophages to pass biological barriers and migrate to inflamed sites. As a comparison, we observed only sporadic positive staining in the control groups (**Figure 2.6d**).

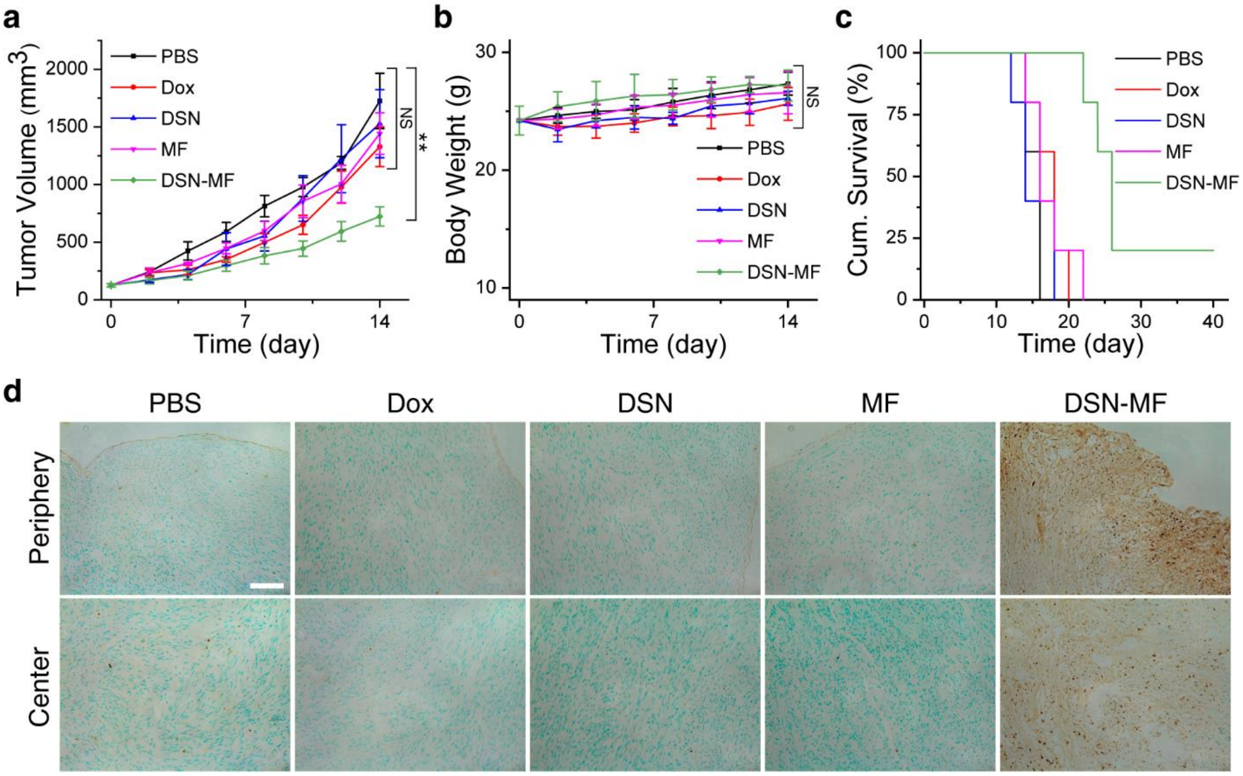

Figure 2.6. Therapy studies with U87MG tumor bearing mice. Animals were randomized to receive one dose i.v. injection of either PBS, free Dox (3 mg Dox kg^{-1}), DSN-52 (3 mg Dox kg^{-1}), RAW264.7 cells (MF, ~4 × 10^6 cells per mouse), or DSN-MF (3 mg Dox kg^{-1}, ~4 × 10^6 cells per mouse). **a)** Tumor growth curves. **b)** Body weight changes. **c)** Kaplan-Meier plot of animal survival. **d)** *In situ* Apoptosis staining (Abcam) analysis of cryo-sectioned tumor tissues at 24 h post treatments. Cytoplasm region was counterstained into green color by methyl green; nuclei of apoptotic cells were counterstained into dark brown dots by diaminobenzidine. Scale bar, 50 μm.

Toxicity studies

We also investigated whether DSN-MF induces systematic toxicity in normal balb/c mice (n = 3). In all Dox related groups (Dox, DSN-52, and DSN-MF), animals showed a small degree of body weight loss on Day 2, but the loss was recovered after 3-5 days (**Figure 2.7a**). Meanwhile, there was no detectable change in rectal temperature for all the treatment groups throughout the study (**Figure 2.7b**). After 7 days, we euthanized the animals and examined major organ tissues by H&E staining. We found a minor elevation of leukocyte infiltration in the alveolar areas in the DSN-MF group, which is likely attributed to the accumulation of exogenous macrophages.[38] No pathological changes were observed in all other organs (**Figure 2.7h**). These include no detection of cardiotoxicity, which is commonly associated with doxorubicin-based treatments. One concern was that too many activated macrophages may cause increased hemophagocytosis, but there was no evidence of this in the spleen (**Figure 2.7h**).

We also examined blood samples taken from the treated animals. For the DSN-MF group, complete blood count (CBC) analysis found that all indices were in the normal ranges. As a comparison, the Dox group showed abnormalities including elevated white blood cell and red blood cell counts, high hemoglobin and mean corpuscular hemoglobin levels, low mean corpuscular volumes, low mature neutrophil counts, and elevated immature neutrophil counts (**Table S5**). These impacts come from hematotoxicity of Dox,[39] which were prevented by selective delivery via macrophages. In addition, we also analyzed protein markers related to inflammation (CRP and TNF-α in **Figure 2.7c, 2.7d**),[40] liver function (AST and ALT in **Figure 2.7e, 2.7f**), and kidney function (BUN in **Figure 2.7g**). Compared to the control, the ALT level was increased in the DSN-MF group (**Figure 2.7f**), though it was still within the normal range.[41] All the other markers are also within the normal ranges.[41] Overall, the histopathology and blood tests confirmed that DSN-MF induced little systematic toxicity to animals.

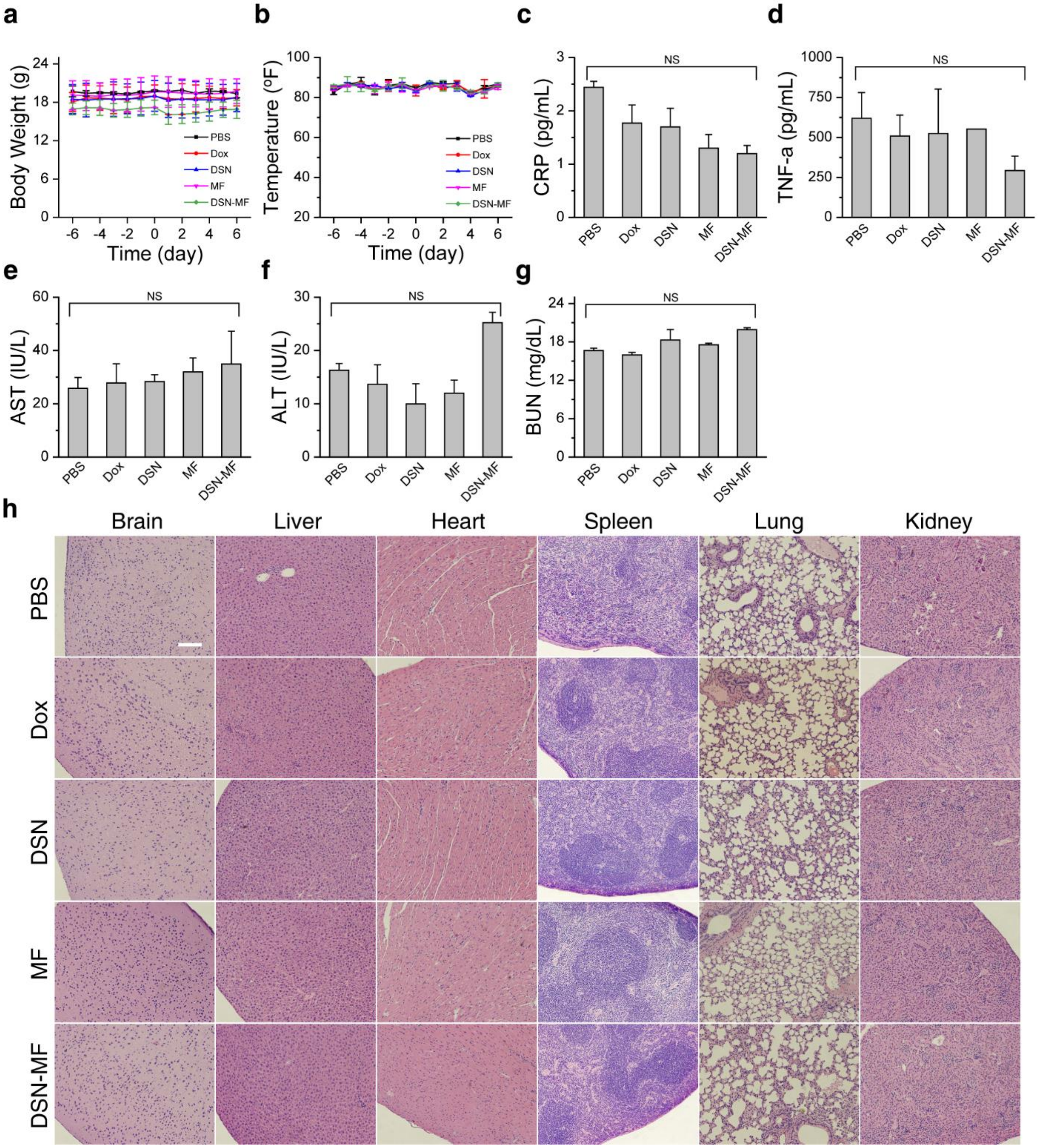

Figure 2.7. Toxicity studies. **a)** Animal body weight changes. **b)** Animal rectal temperature changes. There was a small degree of weight loss in Dox, DSN-52, and DSN-MF group, which was recovered within 5 days. Mice were euthanized on Day 7 for H&E and plasma protein marker analysis: **c)** Plasma CRP, **d)** TNF-α, **e, f)** AST, ALT levels, and **g)** BUN levels. For DSN-

MF, all the indices were in the normal range. **h)** H&E staining of major organs, which were collected on Day 7 post treatments. Except for a small degree of elevated leukocyte infiltration, no pathological changes were observed for the DSN-MF group. Scale bar, 100 μm.

Discussions and conclusion

Inflammation has long been associated with tumor promotion and progression.[42,43] The fact that macrophages or monocytes can respond to chemotactic cues and migrate to inflammation sites has made macrophages a potentially attractive drug delivery vehicle.[22,24] It is envisioned that macrophages can carry therapeutics to tumors, including metastatic sites and tumor central areas, in a highly selective manner. The main challenge of the approach is that it is difficult to load sufficient amounts of drugs onto macrophages. The current study provides a solution. Our drug-nanocapsule minimally releases therapeutics in the first 6-12 h of cell entry, permitting us to hijack macrophages as an efficient vehicle to enrich drugs in tumors without killing them prematurely. In this context, the phagocytic property of macrophages becomes an advantage, allowing for a very high drug loading (e.g. 16.6 pg cell^{-1}) not possible with the conventional "backpack" approach. DSN-MF i.v. injected are first trapped in the lung but afterward gradually migrate to tumors, with a tumor migration rate comparable to untreated macrophages.[44] While many have attempted to load drugs onto live cells for adoptive cell transfer (ACT)[2,7,45,46] (including neutral stem cells and T cells), the more successful examples are seen with using the approach to improve carrier cell survival and functions.[12–14,47] Due to limited drug loading, exploiting ACT to systematically deliver therapeutic drugs has been a challenge. Here we show that DSN-MF can be injected at a clinically relevant chemotherapeutic dose (3 mg kg^{-1}), which again is due to the high drug loading our nanocapsule approach permits. Post-mortem analysis found extensive cell death in tumors, including the central mass (**Figure 2.6d, Figure S7b-c**), confirming the benefits of macrophages-based tumor tropism.

For nanoparticle-based drug delivery, drug accumulation in a tumor and its distribution within it rely almost entirely on passive diffusion. Many nanoparticles after extravasation stay in the tumor peripheral region, never reaching the avascular tumor center. Despite a compromised lymphatic system, these nanoparticles are over time drained into the lymphatic system and cleared from the site. Weissleder et al. observed that in many tumors, nanoparticles are first taken up by local macrophages which serve as a depot for continuous drug release.[48] The group also showed that elevating numbers of macrophages in tumors, for instance by external irradiation, provide strongholds for nanoparticles in tumors, leading to improved drug retention and enhanced therapeutic outcomes.[49] In our strategy, drugs are loaded into macrophages *ex vivo* but similar stronghold effects should have contributed to the treatment.

While the current study is focused on Dox, we anticipate that the platform can be easily extended other therapeutics. Given the high loading capacity of macrophages, it is even possible to use the strategy to deliver a multitude of therapeutics to tumors for combination therapy. Moreover, applications are not limited to cancer therapy. Many other diseases, such as tuberculosis, atherosclerosis, and stroke, are also associated with acute or chronic inflammation. Macrophage-based drug delivery may also hold advantages in the treatment of these diseases. It will be also interesting to test the approach with macrophages derived from autologous monocytes, which is more clinically relevant. It is possible to load nanocapsules into other cell types such as T cells, neural stem cells, and dendritic cells for drug delivery. These possibilities will be explored in future studies.

CHAPTER 3

INCREASING THE MACROPHAGE CONTENT IN TUMOR FOR IMPROVED NANOPARTICLE DELIVERY

Introduction

It has been reported that tumor-associated macrophages (TAMs) can benefit nanoparticle accumulation in tumor tissue by serving as a depot for nanoparticle accumulation[1–4] and remodeling the tumor microenvironment to enhance the extravasation of nanoparticles into the intratumoral interstitium.[5–7]

In this chapter, we aimed to testing this concept on three different tumor models, including murine 4T1 mammary carcinoma model, PC-3 prostate cancer xenograft model, and U-87MG glioblastoma xenograft model. On bilateral tumor models, we specifically increased the macrophage content only on one side tumor by intratumoral injection of RAW264.7 cells. The resulting effect on tumor uptake of nanoparticles could be examined using iron-oxide nanoparticle mediated magnetic resonance imaging (MRI). A following therapy study on subcutaneous tumor model would be conducted to further investigate whether an increased macrophage content can benefit the therapeutic effect using nanomedicine.

From the MR images, we observed a significantly higher accumulation of nanoparticles in U-87MG tumor which was supplemented with additional macrophages than that without any treatment at 4 h. In the therapy study on U-87MG xenografts, the group which received pre-macrophage injection together with Doxove treatment, a liposomal doxorubicin, showed the best tumor suppression result than others. These indicated that an increased macrophage content could benefit the tumor uptake of nanoparticles on this tumor model.

Methods

Chemicals. Doxoves® - stealth liposomal Dox·HCl (2.0 mg mL^{-1}, FormuMax). Molday ION™, 30 nm 30 nm iron oxide-based superparamagnetic (USPIO) T_2 relaxation-darkening MRI contrast agent (Molday).

Cells. RAW264.7 (murine macrophages), 4T1 (murine mammary carcinoma), PC-3 (human prostate cancer), and U87MG (human glioblastoma) were purchased from ATCC. RAW264.7, 4T1, and PC-3 cells were cultured in RPMI1640 medium (Corning, USA) supplemented with 10% FBS (Corning, USA) and 1% penicillin-streptomycin (MediaTech, USA), while U87MG cells were grown in DMEM medium (Corning, USA) supplemented with 10% FBS, 1% non-essential amino acids, and 1% penicillin-streptomycin. All cell lines were incubated under 37 ^{o}C and 5% CO_2 in a humid chamber.

Small animal models. 5-6 week old athymic female nude mice (Harlan) were used for 4T1 murine model and U-87MG xenograft model establishment, while 5-6 week old athymic male nude mice (Harlan) were used for PC-3 xenograft model establishment. Specifically, bilateral subcutaneous model was used for imaging studies by inoculating 1 million cancer cells (i.e., 4T1, PC-3, and U-87MG) onto both the left and right hind leg sites of each mouse. Each group contained 2 mice. For therapy study, 1 million U-87MG cancer cells were inoculated onto the right hind leg site of each mouse. Each group contained 3 mice. The tumor volume was calculated as π/6 × length × $(\text{width})^2$, where length ≥ width.

Imaging studies. When the tumor volume reached 200-250 mm^3, the right side tumor was injected intratumorally with 5 million RAW264.7 cells for each mouse. One day post the macrophage injection, iron oxide nanoparticles, 10 nm, were injected intravenously at 10 mg/kg for each mouse. The mice were scanned on a 7.0 T Varian small animal MRI system before injection of iron oxide nanoparticles, as well as 4 and 24 h after the administration. The scan parameters were the following: TR = 2500 ms, TE = 40 ms, field-of-view (FOV) = 40 mm × 80 mm, matrix size = 2562, thickness = 2 mm. The dark area in tumor was quantified using ImageJ.

Therapy studies. When U-87MG tumor volume reached 75-100 mm^3, 2 million RAW264.7 cells were intratumorally injected into the tumor. One day later, mice were intravenously injected with Doxove at 5 mg/kg. The tumor volume and body weight change of each mouse were monitored daily. Mice were euthanized once the tumor volume was above 1,700 mm^3.

Results

Tumor uptake of iron oxide nanoparticle by T_2 MRI

On U-87MG xenografts, the T_2 MRI signal reduction of the right-side tumor injected with macrophages was observed significantly higher than that of the left-side tumor at 4 h and became comparable at 24 h. The $\%T_2$ signal values of the right and left tumors were 87.99 ± 5.34% (R) and 96.47 ± 5.78% (L) at 4 h ($p = 2.49\%$), and 72.54 ± 10.81% (R) and 74.28 ±

12.84% (L) at 24 h (*p* = 80.47%, **Figure 3.1a-b**). This suggested an increased tumor uptake of iron oxide nanoparticles in the right-side tumor at 4 h.

On murine 4T1 tumor model, a bright area was observed in the MR scan images of the right-side tumor, which may correspond to the presence of necrosis core or aqueous substance and was likely induced by the injection of macrophages (**Figure 3.1c**). The T_2 hypointensity of the right-side tumor was enhanced compared to the left-side one at 4 h but the difference was not significant (R: 61.03 ± 5.17%, L: 65.74 ± 11.75%, *p* = 39.88%), while at 24 h the hypointensity values were significantly different between the right and left tumors (R: 68.48 ± 1.50%, L: 75.62 ± 3.16%, *p* = 0.15%, **Figure 3.1d**). This suggested that the tumor uptake of iron oxide nanoparticles could be more significantly boosted at 24 h on 4T1 model.

On PC-3 xenograft model, there was no significant difference between the left and right tumors at 4 and 24 h in terms of the %T_2 signal change (**Figure 3.1e**). The %T_2 signal values were 75.83 ± 12.42% (R) and 71.38 ± 12.87% (L) at 4 h (*p* = 55.59%), and 111.06 ± 19.04% (R) and 104.76 ± 21.66% (L) at 24 h (*p* = 40.67%, **Figure 3.1f**). The high signal intensity at 24 h indicated a small number of iron oxide nanoparticles deposited in tumor at late time points for PC-3 xenograft tumors.

Therapy study

The imaging study indicated that U-87MG xenograft model could be most benefited from the macrophage supplementation in terms of increasing the tumor deposition of nanoparticles. Therefore, the therapy study was conducted on subcutaneous U-87MG xenograft model. As shown in **Figure 3.2**, tumors injected with macrophages only was observed growing more rapidly than the control group. Meantime, tumors received macrophage injection and Doxove treatment showed the best tumor suppression than others.

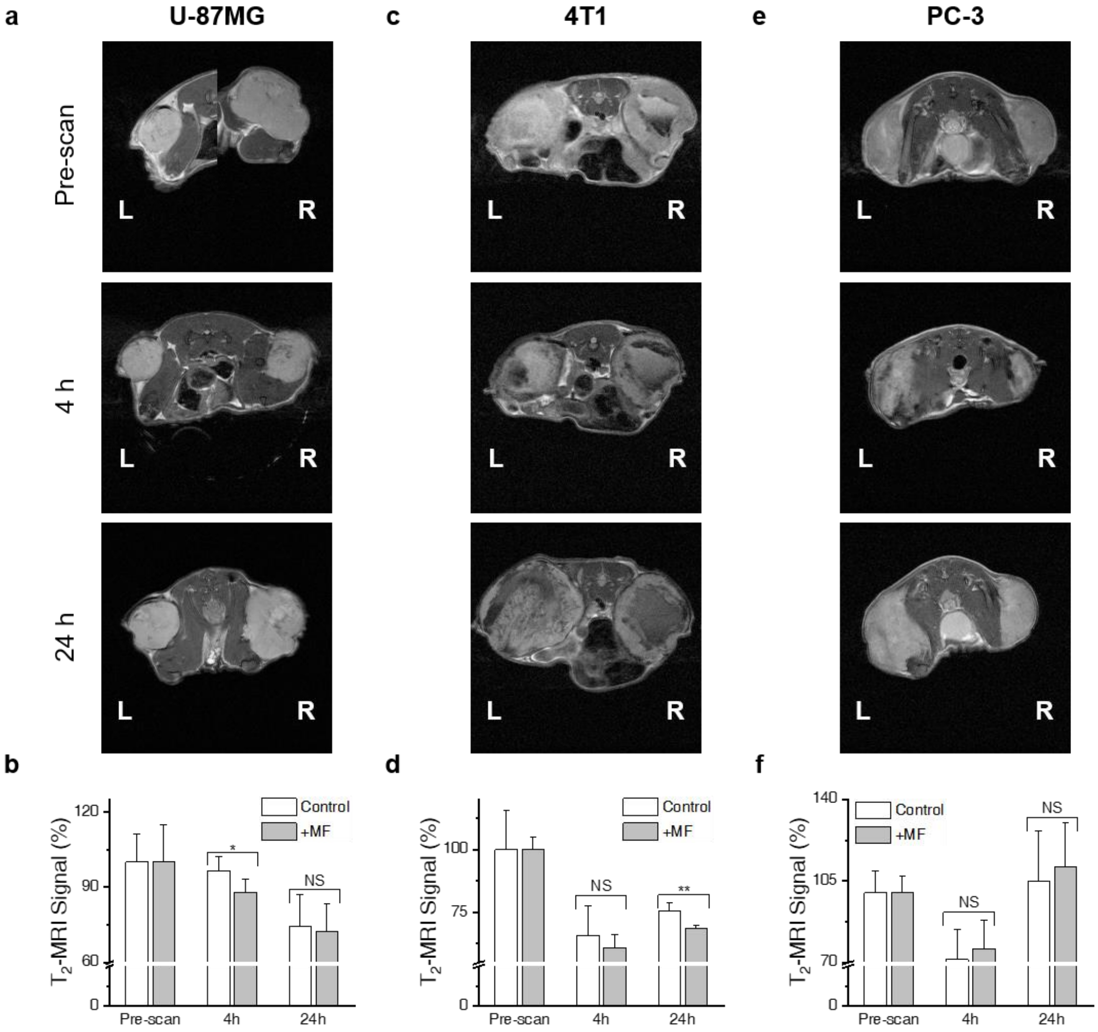

Figure 3.1. Tumor uptake of iron oxide nanoparticles. **a, c, e:** Representative axial MR scan images of bilateral U-87MG xenograft, 4T1, and PC-3 xenograft models. The right-side tumors (R) were pre-injected with macrophages, and the left-side tumors (L) served as a comparison. **b, d, f:** %T_2 MRI signal of the left- and right-side tumors at the corresponding time points by using the following equation: %T_2 MRI signal = the mean value of signal by pixels of the tumor area

of interest at certain time point / the mean value of signal by pixels of the Pre-scanned, corresponding-side tumor area.

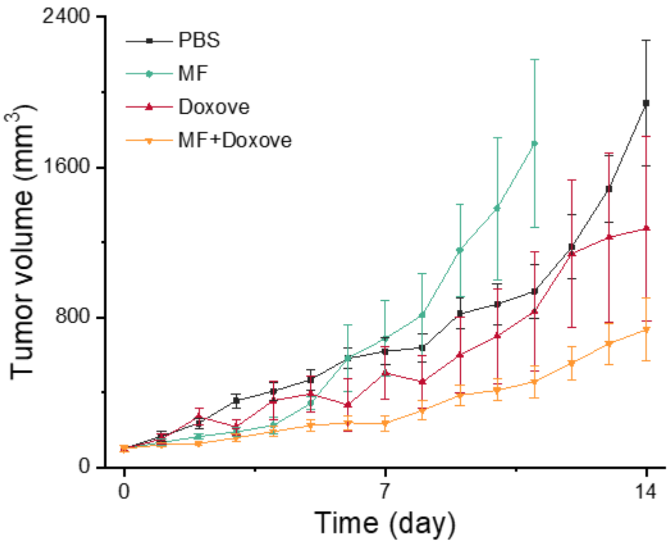

Figure 3.2. Tumor growth curves during the treatment course.

Discussion

Iron oxide nanoparticles have been exploited as a good model nanomedicine to predict the post-administration fate of other therapeutic nanoparticles[8]. In this study, different tumor models showed different tumor deposition behavior of iron oxide nanoparticles post supplementing one tumor with macrophages via intratumoral injection, as illustrated in the T_2 MR scans. This might be attributed to many reasons. First, tumors typically grew at different rates, even for the bilateral tumors developed on the same host. This led to significant size difference between left and right tumors, making it hard to develop a rigidly fair comparison.

Second, owing to the difference on tumor models used in this study (i.e., subcutaneous model vs. xenograft model) as well as cancer type variation, different tumors might develop distinct properties (e.g., tumor permeability, intratumoral vasculature, etc.) and respond to the treatment differently. For instance, 4T1 tumor was found richer in intratumoral vasculature than the other two models, and PC-3 tumor was known by its heterogeneity and poor permeability[9]. Therefore, further studies are required to better understand the mechanism behind.

For the therapy study, the superior tumor suppression by supplementation with macrophages followed with Doxove treatment was considered mainly as a result of enhanced tumor deposition of therapeutic nanoparticles. However, macrophage-mediated programmed cell removal might also be activated in this process, which requires further scrutinization in the future studies. It was also observed that injection of macrophages contributed to promoting tumor growth in the late stages. This might indicate the macrophages were repolarized to the tumorigenic M2 subtypes, which promoted the tumor growth.

CHAPTER 4

NANOPARTICLE-LADEN MACROPHAGES FOR ENHANCED IMMUNOGENECITY AGAINST TUMOR BY PROMOTING THE IMMUNOGENIC CELL DEATH

Introduction

Clinical evidence shows that immunogenic cell death (ICD) of tumor cells induced by some chemotherapy or photoimmunotherapy (PIT) plays an important role in generating adaptive antitumor immunity.[1,2] One key characteristic of ICD that differentiates it from non-immunogenic cell death (NICD) is the generation of damage-associated molecular patterns (DAMPs), such as the endoplasmic reticulum chaperone calreticulin (CRT), ATP, high mobility group box 1 (HMGB1), etc.[3,4] These signals help activate the antigen-presenting cells (APCs) in tumor tissue, promote the presentation of antigens from the dead tumor cells, and elicit strong immunity against other living tumor cells.

Macrophages are considered as a candidate tool to enhance ICD process inside tumor. As a member of professional APCs, macrophages can sense DAMPs produced by tumor cells undergoing ICD for programmed cell removal, antigen presentation, and the following T cell response initiation.[5,6] Meantime, macrophages can also shed CRT into the extracellular space to enhance the ICD-driving cell clearance, and this process is found associated with TLR activation.[7,8] In addition, macrophages treated with agents with ICD inducing or pro-inflammatory ability can serve as a reactor to produce DAMPs (e.g., ATP).[9–11]

In this chapter, we aim to engineer macrophages with a nanoparticle-type ICD inducer into a cellular reactor that can specific-migrate to tumor tissue and produce DAMPs *in situ* to promote the ICD-driving anti-tumor immune response. Compared to other ICD inducing strategies, nanoparticle treatment is relatively simple and capable of inducing a prolonged effect on macrophages. To achieve this, three different kinds of nanoparticles are tested on macrophages to select the lead formulation which can initiate the DAMP production on macrophages without inducing significant adverse effect on cells. Then the engineered macrophages will be administrated to the tumor bearing mice (patient) via either intratumoral injection (proof-of-concept study) or intravenous injection (future study). To make ICD induction beneficial to the prognosis,[8] pre-treatment using ionizing radiation or chemotherapeutic drugs may be required to generate neoantigens of tumor cells or stroma cells.

Given that ICD is recognized as an important mechanism for anti-tumor immunotherapy, it is significantly important to develop strategies to enhance this process in tumor in order to maximize the therapeutic efficacy of combination cancer immunotherapies. Owing to great plasticity, tumor tropic feature, and the important roles in programmed cell removal and antigen presentation, macrophages can serve as a powerful tool for anti-tumor immunotherapy. To the best of my knowledge, no one has tried to engineer macrophages into a DAMPs delivery system for *in situ* production to enhance ICD in tumor. Meantime, many types of nanoparticles can induce endoplasmic reticulum (ER) stress or TLR signaling activation. Therefore, it is reasonable to exploit nanoparticles as the ICD inducer.

Methods

Chemicals. Iron oxide nanopowder (Sigma-Aldrich 544884). Zinc oxide nanoparticle dispersion (Sigma-Aldrich 721077). Aluminum oxide nanopowder (Sigma-Aldrich 544833).

Cells. RAW264.7 (murine macrophages) and CT26 (murine colon carcinoma) cells were purchased from ATCC. Both cell lines were grown in RPMI1640 medium (Corning, USA) supplemented with 10% FBS (Corning, USA) and 1% penicillin-streptomycin (MediaTech, USA), Cells were cultured under 37 ^{o}C and 5% CO_2 in a humid chamber.

Macrophage treatment. RAW264.7 cells were treated with different nanoparticle formulations at various concentrations for 2 h followed with washing and re-supplementation of fresh medium. The cell viability was determined at 24 h post nanoparticle treatment via 3-(4,5-dimethythiazon-2-yl)-2,5-diphenyltetrazolium bromide (MTT) assay. The ATP production and secretion post treatment were measured via ATPlite 1step luminescence assay (PerkinElmer). The released HMGB1 was quantified using mouse HMG1/HMGB1 ELISA kit (LSBio, LS-F11642). The surface expression of CRT was quantified by flow cytometry with anti-CRT antibody with Alexa Fluor®647 (Abcam, ab196159).

Small animal study. 5-6 week old female balb/c mice (Envigo) were used for subcutaneous CT26 murine model establishment. Specifically, 1 million CT26 cancer cells were inoculated onto the right hind leg site for tumor development. Each group contained 3 mice (preliminary study stage). The tumor size was measured and calculated as $\pi/6 \times \text{length} \times (\text{width})^2$, where length $\geq$ width. Treatment started when tumor size reached ~75 mm^3 (Day 0). Specifically, mice were divided randomly into 10 groups: group #1: PBS control; group #2~5: mice received intratumoral injection of 5 million RAW264.7 cells (MF), RAW264.7 cells treated with iron oxide nanoparticles (MF-IO), cells treated with zinc oxide nanoparticles (MF-ZO), and cells treated with aluminum oxide nanoparticles (MF-AO) respectively on Day 0 and 7; group #6: mice received 5 Gy ionizing radiation treatment on tumor site using Mini-X X-ray tube (Ametek) on Day 0 and 7; group #7~10: mice received 5 Gy ionizing radiation treatment on Day 0 and 7, followed with intratumoral injection of 5 million MF, MF-IO, MF-ZO, and MF-AO on the corresponding treatment day respectively. Animals were euthanized on Day 15 and tumors were dissected for further histological and flow cytometry studies (in the future).

Results

Cell viability change post nanoparticle treatment

The cell viability of macrophages was measured at 24 h post treatment with three different nanoparticles. Iron oxide (Fe_2O_3) and aluminum oxide (Al_2O_3) nanoparticles showed little cytotoxicity on RAW264.7 cells at a concentration lower than 100 mg/L, while zinc oxide (ZnO) nanoparticles started to show obvious toxicity at higher concentration with an IC_{50} around 51 mg/L (**Figure 4.1a**). This finding was consistent with two previous literatures.[12,13]

ATP secretion and surface CRT expression

To evaluate the ability of these three nanoparticles in terms of ICD induction, three canonical markers of ICD were measured post treatment, including ATP secretion, surface CRT expression, and HMGB1 release. The data for HMGB1 release is not available at this time point and will be repeated in the future. At 24 h post nanoparticle treatment, the ATP secretion was measured by quantifying the amount of ATP in the culture medium supernatant. As shown in **Figure 4.1b**, all three nanoparticles were observed capable of increasing the ATP secretion compared to the control. The ATP release peaked at 40 mg/L for Fe_2O_3 nanoparticles, 80 mg/L for Al_2O_3 nanoparticles, and 5 mg/L for ZnO nanoparticles respectively. Then the surface CRT level was measured via flow cytometry and quantified by mean fluorescence intensity (MFI). As shown in **Figure 4.1c,** the MFI values for cells treated with 40 mg/L Fe_2O_3 nanoparticles (MF-IO) and 5 mg/L ZnO nanoparticles (MF-ZO) were 32.8 and 22.0 respectively, higher than the untreated cells (MFI = 19.9). The MFI for 80 mg/L Al_2O_3 nanoparticle treated cells (MF-AO) was 14.7.

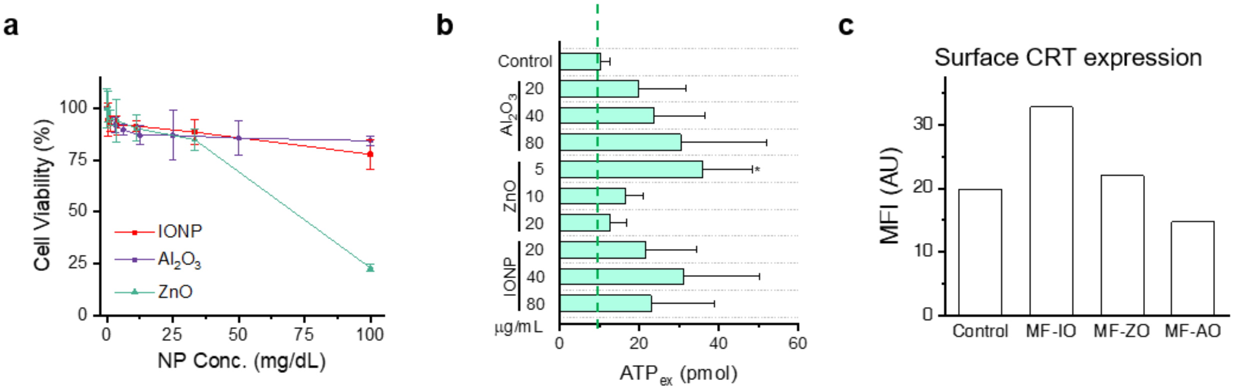

Figure 4.1. **a:** Cell viability of RAW264.7 cells by MTT assay measured at 24 h post treatment with Fe_2O_3 nanoparticles (IONP), Al_2O_3 nanoparticles, and ZnO nanoparticles at various concentrations. **b**: ATP secretion of RAW264.7 cells measured at 24 h post nanoparticle treatment. **c**: mean fluorescence intensity (MFI) of different cell populations labeled with Alexa Fluor®647 conjugated anti-CRT antibodies.

Future Plan

A therapy study to investigate whether the treated macrophages can enhance the anti-tumor immunogenicity is currently in progress, as described in the method session. Flow cytometry, immunohistochemistry (IHC), and immunofluorescence (IF) analysis will be used to examine the post-treatment status changes of different cell populations, including the ratio between infiltrated cytotoxic T cells ($CD44^+CD3^+CD8^+IFN\gamma^+$), regulatory T cells ($CD4^+FoxP3^+CTLA4^+CD103^+$), memory T cells ($CD3^+CD4^+CD62^+CD44^+$), activation of dendritic cells ($CD11c^+CD83^+MHC\text{-}II^+$), natural killer cells ($NK1.1^+$), and macrophages (M1: $F4/80^+CD11b^+iNOS^+$, and M2: $F4/80^+CD11b^+CD206^+Arg1^+$). Post-mortem tissue analysis will also be conducted, including standard H&E staining, tissue collagen content quantification, and apoptosis staining.

In the future, the ovalbumin (OVA)-transfected cancer cell line will be used to further confirm the successful induction of ICD and initiation of cross presentation of antigens. In this part, OVA will serve as a marker for antigen presentation, which can be examined by IHC or flow cytometry using antibodies targeting the SIINFEKL-MHC-II. After parameter optimization, further therapy studies will be conducted using intravenous injection of macrophages and making combinations with other therapies with other regimens.

REFERENCE

CHAPTER 1:

[1] R. B. Rock, G. Gekker, S. Hu, W. S. Sheng, M. Cheeran, J. R. Lokensgard, P. K. Peterson, *Clin. Microbiol. Rev.* **2004**, *17*, 942.

[2] C. T. Ambrose, *Cell. Immunol.* **2006**, *240*, 1.

[3] S. H. E. Kaufmann, *Nat. Immunol.* **2008**, *9*, 705.

[4] J.-M. Cavaillon, S. Legout, *Microbes Infect.* **2016**, *18*, 577.

[5] L. Cassetta, J. W. Pollard, *Nat. Rev. Drug Discov.* **2018**, *17*, 887.

[6] F. Ginhoux, S. Jung, *Nat. Rev. Immunol.* **2014**, *14*, 392.

[7] S. Gordon, P. R. Taylor, *Nat. Rev. Immunol.* **2005**, *5*, 953.

[8] C. Varol, A. Mildner, S. Jung, *Annu. Rev. Immunol.* **2015**, *33*, 643.

[9] D. M. Mosser, J. P. Edwards, *Nat. Rev. Immunol.* **2008**, *8*, 958.

[10] V. A. Adamenko, G. A. Mirskikh, *CriMiCo 2012 - 2012 22nd Int. Crime. Conf. Microw. Telecommun. Technol. Conf. Proc.* **2012**, 133.

[11] S. Gordon, *Cell* **2002**, *111*, 927.

[12] X. Zhang, D. M. Mosser, *J. Pathol.* **2008**, *214*, 161.

[13] A. Iwasaki, R. Medzhitov, *Science (80-.).* **2010**, *327*, 291.

[14] L. Boutens, R. Stienstra, *Diabetologia* **2016**, *59*, 879.

[15] S. K. Biswas, A. Mantovani, *Nat. Immunol.* **2010**, *11*, 889.

[16] C. B. Williams, E. S. Yeh, A. C. Soloff, *npj Breast Cancer* **2016**, *2*, 15025.

[17] C. E. Lewis, J. W. Pollard, *Cancer Res.* **2006**, *66*, 605.

[18] M. Zhang, Y. He, X. Sun, Q. Li, W. Wang, A. Zhao, W. Di, *J. Ovarian Res.* **2014**, *7*, 19.

[19] J. G. Quatromoni, E. Eruslanov, *Am. J. Transl. Res.* **2012**, *4*, 376.

[20] Y. Singh, V. K. Pawar, J. G. Meher, K. Raval, A. Kumar, R. Shrivastava, S. Bhadauria, M. K. Chourasia, *J. Control. Release* **2017**, *254*, 92.

[21] R. Zaynagetdinov, T. P. Sherrill, V. V. Polosukhin, W. Han, J. A. Ausborn, A. G. McLoed, F. B. McMahon, L. A. Gleaves, A. L. Degryse, G. T. Stathopoulos, F. E. Yull, T. S. Blackwell, *J. Immunol.* **2011**, *187*, 5703.

[22] T. Okamoto, T. Sanda, K. Asamitsu, *Curr. Pharm. Des.* **2007**, *13*, 447.

[23] A. E. Powell, E. C. Anderson, P. S. Davies, A. D. Silk, C. Pelz, S. Impey, M. H. Wong, *Cancer Res.* **2011**, *71*, 1497.

[24] X. Lu, Y. Kang, *Cancer Res.* **2009**, *69*, 8536.

[25] Y. Kato, S. Ozawa, C. Miyamoto, Y. Maehata, A. Suzuki, T. Maeda, Y. Baba, *Cancer Cell Int.* **2013**, *13*, 1.

[26] M. Hollmén, F. Roudnicky, S. Karaman, M. Detmar, *Sci. Rep.* **2015**, *5*, 1.

[27] A. Mantovani, S. Sozzani, M. Locati, P. Allavena, A. Sica, *Trends Immunol.* **2002**, *23*, 549.

[28] M. De Palma, C. E. Lewis, *Cancer Cell* **2013**, *23*, 277.

[29] W. E. Mesker, J. M. C. Junggeburt, K. Szuhai, P. de Heer, H. Morreau, H. J. Tanke, R. A. E. M. Tollenaar, *Cell. Oncol.* **2007**, *29*, 387.

[30] S. P. Arlauckas, S. B. Garren, C. S. Garris, R. H. Kohler, J. Oh, M. J. Pittet, R. Weissleder, R. Weissleder, *Theranostics* **2018**, *8*, 5842.

[31] N. Mukaida, T. Nosaka, Y. Nakamoto, T. Baba, *Int. J. Mol. Sci.* **2018**, *20*, 116.

[32] J. Ding, W. Jin, C. Chen, Z. Shao, J. Wu, *PLoS One* **2012**, *7*, e41942.

[33] S. F. Bakhoum, B. Ngo, A. M. Laughney, J.-A. Cavallo, C. J. Murphy, P. Ly, P. Shah, R. K. Sriram, T. B. K. Watkins, N. K. Taunk, M. Duran, C. Pauli, C. Shaw, K. Chadalavada, V. K. Rajasekhar, G. Genovese, S. Venkatesan, N. J. Birkbak, N. McGranahan, M. Lundquist, Q. LaPlant, J. H. Healey, O. Elemento, C. H. Chung, N. Y. Lee, M. Imielenski, G. Nanjangud, D. Pe'er, D. W. Cleveland, S. N. Powell, J. Lammerding, C. Swanton, L. C. Cantley, *Nature* **2018**, *553*, 467.

[34] S. F. Schoppmann, P. Birner, J. Stöckl, R. Kalt, R. Ullrich, C. Caucig, K. Nagy, K. Alitalo, D. Kerjaschki, *Am. J. Pathol.* **2002**, *161*, 947.

[35] T. Niki, S. Iba, M. Tokunou, T. Yamada, Y. Matsuno, S. Hirohashi, *Clin. Cancer Res.* **2000**, *6*, 2431.

[36] M. E. Kaijen-Lambers, J. G. Aerts, T. van Hall, M. van Nimwegen, F. Dammeijer, R. W. Hendriks, K. Bezemer, L. A. Lievense, J. P. Hegmans, *Cancer Immunol. Res.* **2017**, *5*, 535.

[37] P. Perri, D. Di Paolo, C. Brignole, M. Ponzoni, F. Pastorino, *Int. J. Mol. Sci.* **2018**, *19*, 1953.

[38] P. Dhupkar, N. Gordon, J. Stewart, E. S. Kleinerman, *Cancer Med.* **2018**, *7*, 2654.

[39] J. E. Rayahin, J. S. Buhrman, Y. Zhang, T. J. Koh, R. a. Gemeinhart, *ACS Biomater. Sci. Eng.* **2015**, *1*, 481.

[40] D. B. Lyle, J. C. Breger, L. F. Baeva, J. C. Shallcross, C. N. Durfor, N. S. Wang, J. J. Langone, *J. Biomed. Mater. Res. - Part A* **2010**, *94*, 893.

[41] M. Feng, J. Y. Chen, R. Weissman-Tsukamoto, J.-P. Volkmer, P. Y. Ho, K. M. McKenna, S. Cheshier, M. Zhang, N. Guo, P. Gip, S. S. Mitra, I. L. Weissman, *Proc. Natl. Acad. Sci.*

2015, *112*, 2145.

[42] L. Chen, Z. He, L. Qin, Q. Li, X. Shi, S. Zhao, L. Chen, N. Zhong, X. Chen, *PLoS One* **2011**, *6*, e24407.

[43] S. Kaczanowska, A. M. Joseph, E. Davila, *J. Leukoc. Biol.* **2013**, *93*, 847.

[44] S. F. Johnson, S. Lazo, J. L. Guerriero, A. Letai, S. P. Davis, R. D. Carrasco, M. A. Nolan, S. Schad, A. Sotayo, M. Lobera, R. T. Bronson, A. L. Pourzia, J. A. Castrillon, H. E. Ponichtera, *Nature* **2017**, *543*, 428.

[45] M. Pink, D. G. Winkler, S. Gorjestani, C. C. Figueiredo, V. J. Palombella, M. Karin, M. Rausch, N. Ralainirina, J. A. Varner, E. E. W. Cohen, G. Woo, A. V. Nguyen, C. J. Leem, X. Wu, K. A. Frazer, P. Foubert, M. M. Kaneda, J. Kutok, M. C. Schmid, H. Li, K. McGovern, K. S. Messer, R. Sasik, *Nature* **2016**, *539*, 437.

[46] T. Hagemann, T. Lawrence, I. McNeish, K. A. Charles, H. Kulbe, R. G. Thompson, S. C. Robinson, F. R. Balkwill, *J. Exp. Med.* **2008**, *205*, 1261.

[47] R. Ortega, W. Barham, K. Sharman, O. Tikhomirov, T. Giorgio, F. Yull, *Int. J. Nanomedicine* **2016**, *11*, 2163.

[48] C. H. Ries, A. Kiialainen, C.-H. Ooi, M. L. Squadrito, D. Thompson, C. Baer, D. Laoui, S. Hoves, M. De Palma, S. K. Hansen, *Nat. Cell Biol.* **2016**, *18*, 790.

[49] A. M. Georgoudaki, K. E. Prokopec, V. F. Boura, E. Hellqvist, S. Sohn, J. Östling, R. Dahan, R. A. Harris, M. Rantalainen, D. Klevebring, M. Sund, S. E. Brage, J. Fuxe, C. Rolny, F. Li, J. V. Ravetch, M. C. I. Karlsson, *Cell Rep.* **2016**, *15*, 2000.

[50] Z. Huang, Z. Zhang, Y. Jiang, D. Zhang, J. Chen, L. Dong, J. Zhang, *J. Control. Release* **2012**, *158*, 286.

[51] X. Miao, X. Leng, Q. Zhang, *Int. J. Mol. Sci.* **2017**, *18*, DOI 10.3390/ijms18020336.

[52] S. Zanganeh, G. Hutter, R. Spitler, O. Lenkov, M. Mahmoudi, A. Shaw, J. S. Pajarinen, H. Nejadnik, S. Goodman, M. Moseley, L. M. Coussens, H. E. Daldrup-Link, *Nat. Nanotechnol.* **2016**, DOI 10.1038/nnano.2016.168.

[53] X. Chen, G. Chen, W. Zhang, G. Liu, M. Jiang, X. Wu, L. Su, Y. Zhang, *Small* **2015**, *11*, 4191.

[54] S. P. Mukherjee, O. Bondarenko, P. Kohonen, F. T. Andón, T. Brzicová, I. Gessner, S. Mathur, M. Bottini, P. Calligari, L. Stella, E. Kisin, A. Shvedova, R. Autio, H. Salminen-Mankonen, R. Lahesmaa, B. Fadeel, *Sci. Rep.* **2018**, *8*, 1.

[55] A. K. Fuchs, T. Syrovets, K. A. Haas, C. Loos, A. Musyanovych, V. Mailänder, K. Landfester, T. Simmet, *Biomaterials* **2016**, *85*, 78.

[56] H. Y. Tan, N. Wang, S. Li, M. Hong, X. Wang, Y. Feng, *Oxid. Med. Cell. Longev.* **2016**, *2016*, DOI 10.1155/2016/2795090.

[57] Y. Zhang, S. Choksi, K. Chen, Y. Pobezinskaya, I. Linnoila, Z. G. Liu, *Cell Res.* **2013**, *23*, 898.

[58] C. Nathan, A. Cunningham-Bussel, *Nat. Rev. Immunol.* **2013**, *13*, 349.

[59] A. R. Mantegazza, A. Savina, M. Vermeulen, L. Pérez, J. Geffner, O. Hermine, S. D. Rosenzweig, F. Faure, S. Amigorena, *Blood* **2008**, *112*, 4712.

[60] C. Shi, T. Liu, Z. Guo, R. Zhuang, X. Zhang, X. Chen, *Nano Lett.* **2018**, *18*, 7330.

[61] S. Wilhelm, A. J. Tavares, Q. Dai, S. Ohta, J. Audet, H. F. Dvorak, W. C. W. Chan, *Nat. Rev. Mater.* **2016**, *1*, 16014.

[62] H. Chen, W. Zhang, G. Zhu, J. Xie, X. Chen, *Nat. Rev. Mater.* **2017**, *2*, 17024.

[63] Q. Dai, S. Wilhelm, D. Ding, A. M. Syed, S. Sindhwani, Y. Zhang, Y. Y. Chen, P. MacMillan, W. C. W. Chan, *ACS Nano* **2018**, *12*, 8423.

[64] M. A. Miller, Y.-R. Zheng, S. Gadde, C. Pfirschke, H. Zope, C. Engblom, R. H. Kohler, Y. Iwamoto, K. S. Yang, B. Askevold, N. Kolishetti, M. Pittet, S. J. Lippard, O. C. Farokhzad, R. Weissleder, *Nat. Commun.* **2015**, *6*, 8692.

[65] R. M. Schiffelers, J. M. Metselaar, M. H. A. M. Fens, A. P. C. A. Janssen, G. Molema, G. Storm, *Neoplasia* **2005**, *7*, 118.

[66] M. Banciu, R. M. Schiffelers, G. Storm, *Pharm. Res.* **2008**, *25*, 1948.

[67] L. D. Mayer, G. Dougherty, T. O. Harasym, M. B. Bally, *J. Pharmacol. Exp. Ther.* **1997**, *280*, 1406.

[68] M. A. Miller, S. Gadde, C. Pfirschke, C. Engblom, M. M. Sprachman, R. H. Kohler, K. S. Yang, A. M. Laughney, G. Wojtkiewicz, N. Kamaly, S. Bhonagiri, M. J. Pittet, O. C. Farokhzad, R. Weissleder, *Sci. Transl. Med.* **2015**, *7*, 314ra183.

[69] M. Banciu, R. M. Schiffelers, M. H. A. M. Fens, J. M. Metselaar, G. Storm, *J. Control. Release* **2006**, *113*, 1.

[70] T. Tejada-Berges, C. Granai, M. Gordinier, W. Gajewski, *Expert Rev. Anticancer Ther.* **2002**, *2*, 143.

[71] Y. Qie, H. Yuan, C. A. Von Roemeling, Y. Chen, X. Liu, K. D. Shih, J. A. Knight, H. W. Tun, R. E. Wharen, W. Jiang, B. Y. S. Kim, *Sci. Rep.* **2016**, *6*, 1.

[72] Y. Liu, Z. Wang, Y. Liu, G. Zhu, O. Jacobson, X. Fu, R. Bai, X. Lin, N. Lu, X. Yang, W. Fan, J. Song, Z. Wang, G. Yu, F. Zhang, H. Kalish, G. Niu, Z. Nie, X. Chen, *ACS Nano* **2017**, acsnano.7b05908.

[73] W. Zhao, L. Hanson, H.-Y. Lou, M. Akamatsu, P. D. Chowdary, F. Santoro, J. R. Marks, A. Grassart, D. G. Drubin, Y. Cui, B. Cui, *Nat. Nanotechnol.* **2017**, *12*, DOI 10.1038/nnano.2017.98.

[74] S. A. MacParland, K. M. Tsoi, B. Ouyang, X.-Z. Ma, J. Manuel, A. Fawaz, M. A. Ostrowski, B. A. Alman, A. Zilman, W. C. W. Chan, I. D. McGilvray, *ACS Nano* **2016**, acsnano.6b06245.

[75] J. Hoppstädter, M. Seif, A. Dembek, C. Cavelius, H. Huwer, A. Kraegeloh, A. K. Kiemer, *Front. Pharmacol.* **2015**, *6*, 1.

[76] R. Samaniego, A. Dominguez-Soto, M. T. Corcuera, M. Ratnam, A. Puig-Kroger, A. L. Corbi, P. Sanchez-Mateos, E. Sierra-Filardi, F. Gomez-Aguado, *Cancer Res.* **2009**, *69*, 9395.

[77] Y. Luo, *J. Clin. Invest.* **2006**, *116*, 2132.

[78] J. Tang, J. L. Yu, H. Cao, M. Cieslewicz, A. Lieber, E. W. Raines, M. Zavaljevski, S. H. Pun, K. Motoyama, *Proc. Natl. Acad. Sci.* **2013**, *110*, 15919.

[79] M. A. Miller, R. Chandra, M. F. Cuccarese, C. Pfirschke, C. Engblom, S. Stapleton, U. Adhikary, R. H. Kohler, J. F. Mohan, M. J. Pittet, R. Weissleder, *Sci. Transl. Med.* **2017**, *9*, eaal0225.

[80] M. P. Chao, R. Majeti, I. L. Weissman, *Nat. Rev. Cancer* **2012**, *12*, 58.

[81] A. W. Orr, C. E. Pedraza, M. A. Pallero, C. A. Elzie, S. Goicoechea, D. K. Strickland, J. E. Murphy-Ullrich, *J. Cell Biol.* **2003**, *161*, 1179.

[82] V. R. Wiersma, M. Michalak, T. M. Abdullah, E. Bremer, P. Eggleton, *Front. Oncol.* **2015**, *5*, 1.

[83] S. J. Gardai, K. A. McPhillips, S. C. Frasch, W. J. Janssen, A. Starefeldt, J. E. Murphy-Ullrich, D. L. Bratton, P. A. Oldenborg, M. Michalak, P. M. Henson, *Cell* **2005**, *123*, 321.

[84] C. M. Alvey, K. R. Spinler, J. Irianto, C. R. Pfeifer, B. Hayes, Y. Xia, S. Cho, P. C. P. D. Dingal, J. Hsu, L. Smith, M. Tewari, D. E. Discher, *Curr. Biol.* **2017**, *27*, 2065.

[85] Q. Chen, C. Wang, X. Zhang, G. Chen, Q. Hu, H. Li, J. Wang, D. Wen, Y. Zhang, Y. Lu, G. Yang, C. Jiang, J. Wang, G. Dotti, Z. Gu, *Nat. Nanotechnol.* **2018**, *14*, DOI 10.1038/s41565-018-0319-4.

[86] H. Yuan, W. Jiang, C. A. von Roemeling, Y. Qie, X. Liu, Y. Chen, Y. Wang, R. E. Wharen, K. Yun, G. Bu, K. L. Knutson, B. Y. S. Kim, *Nat. Nanotechnol.* **2017**, *12*, 763.

[87] S. Li, S. Feng, L. Ding, Y. Liu, Q. Zhu, Z. Qian, Y. Gu, *Int. J. Nanomedicine* **2016**, *11*, 4107.

[88] L. Yi, H. Xiao, M. Xu, X. Ye, J. Hu, F. Li, M. Li, C. Luo, S. Yu, X. Bian, H. Feng, *J. Neuroimmunol.* **2011**, *232*, 75.

[89] A. Singh, M. Talekar, A. Raikar, M. Amiji, *J. Control. Release* **2014**, *190*, 515.

[90] A. Parodi, N. Quattrocchi, A. L. van de Ven, C. Chiappini, M. Evangelopoulos, J. O. Martinez, B. S. Brown, S. Z. Khaled, I. K. Yazdi, M. V. Enzo, L. Isenhart, M. Ferrari, E. Tasciotti, *Nat. Nanotechnol.* **2013**, *8*, 61.

[91] R. Molinaro, C. Corbo, J. O. Martinez, F. Taraballi, M. Evangelopoulos, S. Minardi, I. K. Yazdi, P. Zhao, E. De Rosa, M. B. Sherman, A. De Vita, N. E. Toledano Furman, X. Wang, A. Parodi, E. Tasciotti, *Nat. Mater.* **2016**, *15*, 1037.

[92] W. Zhang, M. Wang, W. Tang, R. Wen, S. Zhou, C. Lee, H. Wang, W. Jiang, I. M. Delahunty, Z. Zhen, H. Chen, M. Chapman, Z. Wu, E. W. Howerth, H. Cai, Z. Li, J. Xie, *Adv. Mater.* **2018**, *1805557*, 1.

[93] N. L. Klyachko, R. Polak, M. J. Haney, Y. Zhao, R. J. Gomes Neto, M. C. Hill, A. V. Kabanov, R. E. Cohen, M. F. Rubner, E. V. Batrakova, *Biomaterials* **2017**, *140*, 79.

[94] J. Xie, J. Wang, G. Niu, J. Huang, K. Chen, X. Li, X. Chen, *Chem. Commun. (Camb).* **2010**, *46*, 433.

[95] S. J. Madsen, H. M. Gach, S. J. Hong, F. A. Uzal, Q. Peng, H. Hirschberg, *Lasers Surg. Med.* **2013**, *45*, n/a.

[96] Z. Xie, Y. Su, G. B. Kim, E. Selvi, C. Ma, V. Aragon-Sanabria, J.-T. Hsieh, C. Dong, J. Yang, *Small* **2017**, *13*, 1603121.

[97] M. R. Choi, K. J. Stanton-Maxey, J. K. Stanley, C. S. Levin, R. Bardhan, D. Akin, S. Badve, J. Sturgis, J. P. Robinson, R. Bashir, N. J. Halas, S. E. Clare, *Nano Lett.* **2007**, *7*, 3759.

[98] L. Pang, J. Qin, L. Han, W. Zhao, J. Liang, Z. Xie, P. Yang, J. Wang, *Oncotarget* **2016**, *7*, 37081.

[99] E. V. Batrakova, A. V. Kabanov, *J. Drug Deliv. Sci. Technol.* **2013**, *23*, 419.

[100] FDA Approved CAR-macrophage Therapy of Ovarian Cancer into Clinical Trials (https://www.creative-biolabs.com/blog/car-t/fda-approved-car-macrophage-therapy-ovarian-cancer/).

CHAPTER 2:

[1] Q. Wang, H. Cheng, H. Peng, H. Zhou, P. Y. Li, R. Langer, *Adv. Drug Deliv. Rev.* **2015**, *91*, 125.

[2] Y. Su, Z. Xie, G. B. Kim, C. Dong, J. Yang, *ACS Biomater. Sci. Eng.* **2015**, *1*, 201.

[3] A. C. Anselmo, S. Mitragotri, *J. Control. Release* **2014**, *190*, 531.

[4] L. Yi, H. Xiao, M. Xu, X. Ye, J. Hu, F. Li, M. Li, C. Luo, S. Yu, X. Bian, H. Feng, *J. Neuroimmunol.* **2011**, *232*, 75.

[5] A. Singh, M. Talekar, A. Raikar, M. Amiji, *J. Control. Release* **2014**, *190*, 515.

[6] S. Li, S. Feng, L. Ding, Y. Liu, Q. Zhu, Z. Qian, Y. Gu, *Int. J. Nanomedicine* **2016**, *11*, 4107.

[7] M. Ayer, H. A. Klok, *J. Control. Release* **2017**, *259*, 92.

[8] H. Cheng, C. J. Kastrup, R. Ramanathan, D. J. Siegwart, M. Ma, S. R. Bogatyrev, Q. Xu, K. A. Whitehead, R. Langer, D. G. Anderson, *ACS Nano* **2010**, *4*, 625.

[9] L. Li, Y. Guan, H. Liu, N. Hao, T. Liu, X. Meng, C. Fu, Y. Li, Q. Qu, Y. Zhang, S. Ji, L. Chen, D. Chen, F. Tang, *ACS Nano* **2011**, *5*, 7462.

[10] R. Mooney, Y. Weng, E. Garcia, S. Bhojane, L. Smith-Powell, S. U. Kim, A. J. Annala, K. S. Aboody, J. M. Berlin, *J. Control. Release* **2014**, *191*, 82.

[11] R. Mooney, Y. Weng, R. Tirughana-Sambandan, V. Valenzuela, S. Aramburo, E. Garcia, Z. Li, M. Gutova, A. J. Annala, J. M. Berlin, K. S. Aboody, *Futur. Oncol.* **2014**, *10*, 401.

[12] M. J. Mitchell, E. C. Wayne, K. Rana, C. B. Schaffer, M. R. King, *Proc. IEEE Annu. Northeast Bioeng. Conf. NEBEC* **2014**, *2014–Decem*, 1.

[13] E. C. Wayne, S. Chandrasekaran, M. J. Mitchell, M. F. Chan, R. E. Lee, C. B. Schaffer, M. R. King, *J. Control. Release* **2016**, *223*, 215.

[14] S. Chandrasekaran, M. F. Chan, J. Li, M. R. King, *Biomaterials* **2016**, *77*, 66.

[15] A. C. Anselmo, J. B. Gilbert, S. Kumar, V. Gupta, R. E. Cohen, M. F. Rubner, S. Mitragotri, *J. Control. Release* **2015**, *199*, 29.

[16] W. Tang, Z. Zhen, M. Wang, H. Wang, Y.-J. Chuang, W. Zhang, G. D. Wang, T. Todd, T. Cowger, H. Chen, L. Liu, Z. Li, J. Xie, *Adv. Funct. Mater.* **2016**, *26*, 1757.

[17] B. Huang, W. D. Abraham, Y. Zheng, S. C. Bustamante López, S. S. Luo, D. J. Irvine, *Sci. Transl. Med.* **2015**, *7*, 291ra94.

[18] M. T. Stephan, J. J. Moon, S. H. Um, A. Bershteyn, D. J. Irvine, *Nat. Med.* **2010**, *16*, 1035.

[19] A. Parodi, N. Quattrocchi, A. L. van de Ven, C. Chiappini, M. Evangelopoulos, J. O. Martinez, B. S. Brown, S. Z. Khaled, I. K. Yazdi, M. V. Enzo, L. Isenhart, M. Ferrari, E. Tasciotti, *Nat. Nanotechnol.* **2013**, *8*, 61.

[20] R. Molinaro, C. Corbo, J. O. Martinez, F. Taraballi, M. Evangelopoulos, S. Minardi, I. K. Yazdi, P. Zhao, E. De Rosa, M. B. Sherman, A. De Vita, N. E. Toledano Furman, X. Wang, A. Parodi, E. Tasciotti, *Nat. Mater.* **2016**, *15*, 1037.

[21] J. Choi, H. Y. Kim, E. J. Ju, J. Jung, J. Park, H. K. Chung, J. S. Lee, J. S. Lee, H. J. Park, S. Y. Song, S. Y. Jeong, E. K. Choi, *Biomaterials* **2012**, *33*, 4195.

[22] L. Pang, J. Qin, L. Han, W. Zhao, J. Liang, Z. Xie, P. Yang, J. Wang, *Oncotarget* **2016**, *7*, 37081.

[23] W. C. Huang, W. H. Chiang, Y. H. Cheng, W. C. Lin, C. F. Yu, C. Y. Yen, C. K. Yeh, C. S. Chern, C. S. Chiang, H. C. Chiu, *Biomaterials* **2015**, *71*, 71.

[24] J. Xie, J. Wang, G. Niu, J. Huang, K. Chen, X. Li, X. Chen, *Chem. Commun. (Camb).* **2010**, *46*, 433.

[25] E. Scarpa, J. L. Bailey, A. A. Janeczek, P. S. Stumpf, A. H. Johnston, R. O. C. Oreffo, Y. L. Woo, Y. C. Cheong, N. D. Evans, T. A. Newman, *Sci. Rep.* **2016**, *6*, 1.

[26] M. Vandenbranden, G. De Gand, R. Brasseur, F. Defrise-Quertain, J. M. Ruysschaert, *Biosci. Rep.* **1985**, *5*, 477.

[27] S. Zhang, Z. Chu, C. Yin, C. Zhang, G. Lin, Q. Li, *J. Am. Chem. Soc.* **2013**, *135*, 5709.

[28] J. E. DiCiccio, B. E. Steinberg, *J. Gen. Physiol.* **2011**, *137*, 385.

[29] D. M. Mosser, J. P. Edwards, *Nat. Rev. Immunol.* **2008**, *8*, 958.

[30] A. Mantovani, S. Sozzani, M. Locati, P. Allavena, A. Sica, *Trends Immunol.* **2002**, *23*, 549.

[31] C. Soekmadji, C. C. Nelson, *Biomed Res. Int.* **2015**, *2015*, 1.

[32] X. Zhang, X. Yuan, H. Shi, L. Wu, H. Qian, W. Xu, *J. Hematol. Oncol.* **2015**, *8*, 1.

[33] A. S. Azmi, B. Bao, F. H. Sarkar, and F. H. S. Asfar S. Azmi1, Bin Bao, *Cancer Metastasis Rev.* **2014**, *32*, 1.

[34] Q. Quan, J. Xie, H. Gao, M. Yang, F. Zhang, G. Liu, X. Lin, A. Wang, H. S. Eden, S. Lee, G. Zhang, X. Chen, *Mol. Pharm.* **2011**, *8*, 1669.

[35] H. Chen, W. Zhang, G. Zhu, J. Xie, X. Chen, *Nat. Rev. Mater.* **2017**, *2*, 17024.

[36] N. Adonai, N. Adonai, K. N. Nguyen, J. Walsh, M. Iyer, T. Toyokuni, M. E. Phelps, T. McCarthy, D. W. McCarthy, S. S. Gambhir, *Proc. Natl. Acad. Sci.* **2002**, *99*, 3030.

[37] H. Dou, C. J. Destache, J. R. Morehead, R. L. Mosley, M. D. Boska, J. Kingsley, S. Gorantla, L. Poluektova, J. a. Nelson, M. Chaubal, J. Werling, J. Kipp, B. E. Rabinow, H. E. Gendelman, *Blood* **2006**, *108*, 2827.

[38] U. M. Fischer, M. T. Harting, F. Jimenez, W. O. Monzon-Posadas, H. Xue, S. I. Savitz, G. A. Laine, C. S. Cox, *Stem Cells Dev.* **2009**, *18*, 683.

[39] D. A. Eppstein, C. G. Kurahara, N. A. Bruno, T. G. Terrell, *Cancer Res.* **1989**, *49*, 3955.

[40] MOUSE C-REACTIVE PROTEIN (CRP) ELISA Life Diagnostics , Inc. (lifediagnostics.com)

[41] S. Chen, G. Li, K. Zhu, P. Sun, R. Wang, X. Zhao, *Oncol. Lett.* **2014**, *7*, 250.

[42] L. M. Coussens, Z. Werb, *Nature* **2002**, *420*, 860.

[43] H. F. Dvorak, *Cancer Immunol. Res.* **2015**, *3*, 1.

[44] H. Dou, C. J. Destache, J. R. Morehead, R. L. Mosley, M. D. Boska, J. Kingsley, S. Gorantla, L. Poluektova, J. a. Nelson, M. Chaubal, J. Werling, J. Kipp, B. E. Rabinow, H. E. Gendelman, *Blood* **2006**, *108*, 2827.

[45] Z. Xie, Y. Su, G. B. Kim, E. Selvi, C. Ma, V. Aragon-Sanabria, J.-T. Hsieh, C. Dong, J. Yang, *Small* **2017**, *13*, 1603121.

[46] E. V. Batrakova, H. E. Gendelman, A. V. Kabanov, *Expert Opin Drug Deliv* **2011**, *8*, 415.

[47] S. Lee, E. Choi, M.-J. Cha, K.-C. Hwang, *Oxid. Med. Cell. Longev.* **2015**, *2015*, 1.

[48] J. Kim, J. E. Lee, J. Lee, J. H. Yu, B. C. Kim, K. An, Y. Hwang, C.-H. Shin, J.-G. Park, J. Kim, T. Hyeon, *J. Am. Chem. Soc.* **2006**, *128*, 688.

[49] M. A. Miller, R. Chandra, M. F. Cuccarese, C. Pfirschke, C. Engblom, S. Stapleton, U. Adhikary, R. H. Kohler, J. F. Mohan, M. J. Pittet, R. Weissleder, *Sci. Transl. Med.* **2017**, *9*, eaal0225.

CHAPTER 3:

[1] Q. Dai, S. Wilhelm, D. Ding, A. M. Syed, S. Sindhwani, Y. Zhang, Y. Y. Chen, P. MacMillan, W. C. W. Chan, *ACS Nano* **2018**, *12*, 8423.

[2] M. A. Miller, Y.-R. Zheng, S. Gadde, C. Pfirschke, H. Zope, C. Engblom, R. H. Kohler, Y. Iwamoto, K. S. Yang, B. Askevold, N. Kolishetti, M. Pittet, S. J. Lippard, O. C. Farokhzad, R. Weissleder, *Nat. Commun.* **2015**, *6*, 8692.

[3] R. M. Schiffelers, J. M. Metselaar, M. H. A. M. Fens, A. P. C. A. Janssen, G. Molema, G. Storm, *Neoplasia* **2005**, *7*, 118.

[4] M. Banciu, R. M. Schiffelers, G. Storm, *Pharm. Res.* **2008**, *25*, 1948.

[5] L. D. Mayer, G. Dougherty, T. O. Harasym, M. B. Bally, *J. Pharmacol. Exp. Ther.* **1997**,

280, 1406.

[6] M. A. Miller, S. Gadde, C. Pfirschke, C. Engblom, M. M. Sprachman, R. H. Kohler, K. S. Yang, A. M. Laughney, G. Wojtkiewicz, N. Kamaly, S. Bhonagiri, M. J. Pittet, O. C. Farokhzad, R. Weissleder, *Sci. Transl. Med.* **2015**, *7*, 314ra183.

[7] M. Banciu, R. M. Schiffelers, M. H. A. M. Fens, J. M. Metselaar, G. Storm, *J. Control. Release* **2006**, *113*, 1.

[8] H. Chen, W. Zhang, G. Zhu, J. Xie, X. Chen, *Nat. Rev. Mater.* **2017**, *2*, 17024.

[9] M. T. S. Bertilaccio, M. Grioni, B. W. Sutherland, E. Degl'Innocenti, M. Freschi, E. Jachetti, N. M. Greenberg, A. Corti, M. Bellone, *Prostate* **2008**, *68*, 1105.

CHAPTER 4:

[1] L. Galluzzi, A. Buqué, O. Kepp, L. Zitvogel, G. Kroemer, *Nat. Rev. Immunol.* **2017**, *17*, 97.

[2] M. Ogawa, Y. Tomita, Y. Nakamura, M.-J. Lee, S. Lee, S. Tomita, T. Nagaya, K. Sato, T. Yamauchi, H. Iwai, A. Kumar, T. Haystead, H. Shroff, P. L. Choyke, J. B. Trepel, H. Kobayashi, M. Ogawa, Y. Tomita, Y. Nakamura, M.-J. Lee, S. Lee, S. Tomita, T. Nagaya, K. Sato, T. Yamauchi, H. Iwai, A. Kumar, T. Haystead, H. Shroff, P. L. Choyke, J. B. Trepel, H. Kobayashi, *Oncotarget* **2017**, *8*, 10425.

[3] O. Kepp, L. Senovilla, I. Vitale, E. Vacchelli, S. Adjemian, P. Agostinis, L. Apetoh, F. Aranda, V. Barnaba, N. Bloy, L. Bracci, K. Breckpot, D. Brough, A. Buqué, M. G. Castro, M. Cirone, M. I. Colombo, I. Cremer, S. Demaria, L. Dini, A. G. Eliopoulos, A. Faggioni, S. C. Formenti, J. Fučíková, L. Gabriele, U. S. Gaipl, J. Galon, A. Garg, F. Ghiringhelli, N. A. Giese, Z. S. Guo, A. Hemminki, M. Herrmann, J. W. Hodge, S. Holdenrieder, J.

Honeychurch, H.-M. Hu, X. Huang, T. M. Illidge, K. Kono, M. Korbelik, D. V. Krysko, S. Loi, P. R. Lowenstein, E. Lugli, Y. Ma, F. Madeo, A. A. Manfredi, I. Martins, D. Mavilio, L. Menger, N. Merendino, M. Michaud, G. Mignot, K. L. Mossman, G. Multhoff, R. Oehler, F. Palombo, T. Panaretakis, J. Pol, E. Proietti, J.-E. Ricci, C. Riganti, P. Rovere-Querini, A. Rubartelli, A. Sistigu, M. J. Smyth, J. Sonnemann, R. Spisek, J. Stagg, A. Q. Sukkurwala, E. Tartour, A. Thorburn, S. H. Thorne, P. Vandenabeele, F. Velotti, S. T. Workenhe, H. Yang, W.-X. Zong, L. Zitvogel, G. Kroemer, L. Galluzzi, *Oncoimmunology* **2014**, *3*, e955691.

[4] D. V. Krysko, A. D. Garg, A. Kaczmarek, O. Krysko, P. Agostinis, P. Vandenabeele, *Nat. Rev. Cancer* **2012**, *12*, 860.

[5] M. P. Chao, R. Majeti, I. L. Weissman, *Nat. Rev. Cancer* **2012**, *12*, 58.

[6] S. J. Gardai, K. A. McPhillips, S. C. Frasch, W. J. Janssen, A. Starefeldt, J. E. Murphy-Ullrich, D. L. Bratton, P. A. Oldenborg, M. Michalak, P. M. Henson, *Cell* **2005**, *123*, 321.

[7] K. Lee, M. Rafi, X. Wang, K. Aran, X. Feng, C. Lo Sterzo, R. Tang, N. Lingampalli, H. J. Kim, N. Murthy, *Nat. Mater.* **2015**, DOI 10.1038/nmat4269.

[8] V. R. Wiersma, M. Michalak, T. M. Abdullah, E. Bremer, P. Eggleton, *Front. Oncol.* **2015**, *5*, 1.

[9] X. Cui, B. Wan, Y. Yang, X. Ren, L.-H. Guo, H. Zhang, *Small* **2016**, 5998.

[10] I. Martins, Y. Wang, M. Michaud, Y. Ma, A. Q. Sukkurwala, S. Shen, O. Kepp, D. Métivier, L. Galluzzi, J. L. Perfettini, L. Zitvogel, G. Kroemer, *Cell Death Differ.* **2014**, *21*, 79.

[11] M. J. Smyth, S. F. Ngiow, A. Ribas, M. W. L. Teng, *Nat. Rev. Clin. Oncol.* **2016**, *13*, 143.

[12] H. Zhang, Z. Ji, T. Xia, H. Meng, C. Low-Kam, R. Liu, S. Pokhrel, S. Lin, X. Wang, Y. P.

Liao, M. Wang, L. Li, R. Rallo, R. Damoiseaux, D. Telesca, L. Mädler, Y. Cohen, J. I. Zink, A. E. Nel, *ACS Nano* **2012**, *6*, 4349.

[13] V. Mirshafiee, B. Sun, C. H. Chang, Y. P. Liao, W. Jiang, J. Jiang, X. Liu, X. Wang, T. Xia, A. E. Nel, *ACS Nano* **2018**, *12*, 3836.

APPENDICES

A Supporting information for Chapter 1

Methods

Chemicals. Tetraethyl orthosilicate (TEOS, ≥99.0%, Sigma-Aldrich), ammonium hydroxide (28.0-30.0%, Sigma-Aldrich), ethanol (200 proof, Decon Labs, Inc.), doxorubicin hydrochloride salt (Dox·HCl, LC Labs), Doxoves® - stealth liposomal Dox·HCl (2.0 mg mL^{-1}, FormuMax), hexadecyltrimethylammonium bromide (CTAB, ≥99%, Sigma-Aldrich), ethyl acetate (Fisher Scientific, HPLC Grade), HCl (J.T. Baker, 36.5-38%).

DSN synthesis. Dox-encapsulated silica nanocomplex (DSN) was synthesized by a modified procedure based on a previous study[1]. Different volumes of 4.2-4.5% ammonium hydroxide aqueous solutions (e.g., 0.15 mL, 0.3 mL, 0.6 mL) and TEOS (e.g., 2.5, 5, and 10 μL) were added into ethanol to form a 4.0 mL Dox solution of varied concentrations (e.g., 0.10, 0.25, and 0.50 mg mL^{-1}). The mixture was magnetically stirred at room temperature for 24 hours. The drug-loaded NPs were collected by repeated wash with ethanol and centrifugation (12,000 rpm, 5 min). The as-synthesized particles were lyophilized and stored at -80 ˚C in the dark. Specifically, DSN-0 NP was synthesized using 0.3 mL ammonium hydroxide, 5 μL TEOS, and 0.25 mg Dox mL^{-1}. For silica coating onto DSN-0, the as-synthesized DSN-0 was re-dispersed in 4.0 mL 200 proof ethanol with brief sonication. Then, 0.3 mL ammonium hydroxide solution (4.2-4.5%) and different volumes of TEOS (e.g., 2.5, 5.0, and 10.0 μL) were dropwisely added to the colloidal solution. The mixture was magnetically stirred at room temperature for 24 hours. The coated DSN nanoparticles were washed, collected, lyophilized, and stored at -80 ^{o}C following the same protocol. According to the coating thicknesses measured by TEM, the coated DSNs were designated as DSN-12, DSN-22, and DSN-52, respectively.

Mesoporous silica nanoparticle synthesis. Mesoporous silica nanoparticles were synthesized following a published protocol[2]. Briefly, nanoparticles were prepared by mixing 3 mL TEOS with CTAB (5.5 mM) in a 300 mL, 70 ^{o}C aqueous solution containing 4.2 mmol NaOH, followed with the addition of 18 mL ethyl acetate. Free CTAB was removed by stirring nanoparticles in 100 mL ethanol containing 1 mL 37% HCl at 60 ^{o}C for 3 hours. The as-synthesized nanoparticles were dried at 60 ^{o}C overnight. To load Dox, mesoporous silica nanoparticles were stirred in a Dox ethanol solution (2.5 mg mL^{-1}) overnight at room temperature in the dark. The resulting Dox-encapsulated NPs were washed with water twice, lyophilized, and stored at -80 ˚C.

Characterization of nanoparticles. The morphology, size distributions, zeta potential, and EDS of nanoparticles were characterized by transmission electron microscope (TEM, H-9500), scanning electron microscope (SEM, FEI Teneo), and dynamic light scattering (DLS, Malvern Zetasizer Nano S90). The temporal degradation of nanoparticles at pH 5.0 and 7.4 was examined using TEM. Briefly, nanoparticles dispersed in PBS (pH 5.0 and 7.4) were incubated at 37 ^{o}C under constant shaking for 2, 6, 24, and 72 h. The remaining nanoparticles were collected and examined under TEM for morphology and size changes. Absorbance at 470, 480, 490 nm was used to quantify Dox content. The loading capacity (%LC) was calculated by the following equation: %LC = (Drug loaded)/(nanoparticle weight) × 100%, where the amount of drug loaded was determined by absorbance, and the nanoparticle weight determined either by directly weighing lyophilized nanoparticles or calculating the silica weight based on inductively coupled plasma-optical emission spectrometry (ICP-OES) results. In the latter case, it was assumed that silica dioxide (SiO_2) was the major silica component and that nanoparticle weight = Dox weight + SiO_2 weight. Drug release of different nanoparticle formulations was determined using a Slide-A-Lyzer 10K MWCO mini dialysis device (Thermo Scientific). Briefly, nanoparticles containing the same Dox content were dispersed in 0.5 mL PBS and dialyzed against 14 mL PBS (pH 5.0 and 7.4) at 37 ^{o}C under constant shaking. At different time points (i.e., 0, 0.5, 1, 2, 4, 8, 12. 24, 48, 72, 96, 120 hour), a 0.5 mL PBS exmple from the bottom chamber was collected, which was supplanted with 0.5 mL fresh PBS. Cumulative Dox release over 5 days was quantified by subtracting the remaining Dox in the cassette from the initial loading amount. Dox concentration in the sample solutions were measured by fluorescence spectroscopy analysis (ex/em: 470/590 nm).

***In vitro* cellular loading studies.** RAW264.7 (murine macrophages) and U87MG (human glioblastoma) were purchased from ATCC. RAW264.7 cells were cultured in RPMI1640 medium (Corning, USA) supplemented with 10% FBS (Corning, USA) and 1% penicillin-streptomycin (MediaTech, USA). During the nanoparticle loading stage, FBS-free RPMI1640 medium was used for culturing. U87MG cells were grown in DMEM medium (Corning, USA) supplemented with 10% FBS, 1% non-essential amino acids, and 1% penicillin-streptomycin. These two cell lines were incubated under 37 ^{o}C and 5% CO_2 in a humid chamber. For nanoparticle loading studies, nanoparticles (DSN-22 or DSN-52) of different concentrations (i.e., 0, 10, 20, and 40 μg Dox mL^{-1}) were incubated with RAW264.7 cells for 1, 2, and 4 h, followed with gentle wash with PBS or complete medium. Depending on the purpose of each study, the DSN-laden macrophages were either collected using trypsin treatment or cultured further with complete growth medium. To determine the amount of Dox loaded into cells, DSN-laden cells were counted and then lysed by sonication in PBS (pH 5.0). The amounts of released Dox was measured by spectroscopic analysis. The Dox content on a per cell basis was calculated compared with macrophages without nanoparticle loading. To study whether DSN-52 nanoparticles were laden into cells via internalization, nanoparticles were incubated with RAW264.7 cells under the same condition described above except using 4℃ for incubation and adding 0.1 wt.% NaN_3 (to minimize energy-consuming internalization process). The Dox loading amount on a per cell basis was compared with control. To evaluate the impact of loaded DSNs on macrophages, the viability change was first assessed at different time points post nanoparticle loading by 3-(4,5-dimethythiazon-2-yl)-2,5-diphenyl tetrazolium bromide (MTT) assay or Live/Dead Cytotoxicity assay and the results were compared with normal macrophages. In the end, DSN-52 NPs were selected for cell loading, and the loading process was accomplished by 2-h incubation at a concentration of 20 μg Dox mL^{-1}. All *in vitro* experiments were repeated at least twice.

Cell invasion/migration assay. Cell invasion/migration assay was used to examine whether DSN-laden RAW264.7 (DSN-MF) cells remained tumor-tropic. Unladen RAW264.7 (MF) cells served as controls. A transwell polycarbonate membrane cell culture insert set (Corning, 8.0 μm pore sized) was fitted into a 6-well cell culture plate for this study. Migration assay required coating the upper surface of the inserts with a layer of Matrigel beforehand. For experimental groups, U87MG cells (0.2 million cells) as a lure were seeded to the bottom of each well and cultured overnight. For the control group, only medium was added into each bottom well. Then, 0.4 million DSN-MF cells or normal RAW264.7 cells (dispersed in 1.0 mL FBS-free RPMI1640 medium) were seeded onto the upper chamber of each insert. The transmigration process took 16 hours to accomplish under normal incubation conditions (37 °C, 5% CO_2). Afterwards, the transwell inserts were collected, washed twice with PBS, fixed with formaldehyde (3.7% in PBS) for 2 min, washed twice with PBS again, permeabilized with methanol for 20 min, and subjected to Giemsa staining. Those cells that failed to transmigrate (i.e., remained on top of the film) were scraped off with cotton swabs. Optical and fluorescence images of the transmigrated RAW264.7 cells were captured. Due to Giemsa staining, invaded/migrated cells were blue in bright-field images. In fluorescence images, DSN-MF cells were visualized due to the intrinsic fluorescent properties of Dox. For each sample, 25 images of different areas were acquired for cell counting to obtain a statistically significant result. The experiment was repeated twice.

#	**Upper chamber**	**Assay Type**	**Lower chamber**
1	MF	Invasion	U87MG cells
2			Empty
3		Migration (+ Matrigel)	U87MG cells
4			Empty
5	DSN-MF	Invasion	U87MG cells
6			Empty
7		Migration (+ Matrigel)	U87MG cells
8			Empty

Cell phenotype change study. Enzyme-linked immunosorbent assay (ELISA) were used to examine the cytokine released by macrophages after they were loaded with DSN-52 nanoparticles. Briefly, the medium supernatants from DSN-MF seeded plates were collected at different time points (i.e., 2 and 24 h post loading) to quantify the concentrations of different cytokines, including interleukin-1beta (IL-1β), IL-6, IL-10, IL-12p70, and tumor necrosis factor-α (TNF-α). The results were compared with normal macrophage control groups with the same cell numbers, the same culture medium volumes, and the same culturing conditions. The experiments were conducted by following vendor-provided protocols (RayBiotech) and the concentrations of each cytokine were calculated by comparing to standard calibration curves. All ELISA tests were repeated at least twice.

***In vitro* therapy study.** DSN-MF as well as MF cells were cultured with complete growth medium for 12, 24, and 48 hours (2 million cells, 5 mL medium for each group). Supernatants from each group were collected. The amounts of Dox in the supernatants were assessed by fluorescence spectroscopy analysis with the help of standard calibration curves. To evaluate the cytotoxicity to cancer cells, U87MG cells that were pre-cultured in a separate 6 well plate overnight (confluence ~ 0.4 million cells per well). Supernatants taken DSN-MF cell cultures at 12, 24 h, and 48 h were added into the U87MG cell culture medium. For controls, 1.0 mL complete RPMI1640 medium was added. The viability of U87MG cells at 48 h was examined by MTT assay. For imaging studies to visualize the accumulation of Dox in cancer cells, U87MG cells were co-incubated with different supernatant medium for 6 h, washed with PBS, and then imaged under a fluorescence microscope.

Exosome isolation and analysis. Ten T75 flasks were each seeded with 2 million RAW264.7 cells. After overnight culturing, cells were laden with DSN-52 nanoparticles following above mentioned protocol. The medium supernatant was collected at 45 h post loading. Exosomes in the supernatant were enriched via a series of centrifugation: (1) centrifugation at 300 ×g for 10 min at 4 ºC to remove the living cells, (2) 2000 ×g at 4 ºC for 10 min to remove dead cells, (3) 10,000 ×g at 4 ºC for 30 min to remove the cell debris, (4) a ultracentrifugation step at 100 000 ×g at 4ºC for 90 min, and (5) 100 000 ×g at 4ºC for 60 min after PBS wash. Collected exosomes were dispersed in (1) PBS, (2) DI water, and (3) radioimmunoprecipitation assay (RIPA) buffer. For TEM imaging, 5 μL exosome dispersion in DI water was dropped onto a TEM grid and air-dried for 10 min, followed by addition of 5 μL of 1 wt.% uranyl acetate in DI water for negative staining. The hydrodynamic size of exosomes in PBS was analyzed by DLS after filtration twice through a 0.45 μm filter unit. The amount of Dox in exosome was quantified by measuring Abs at 470 nm and comparing to a calibration curve. Alternatively, Dox was quantified by measuring fluorescence with excitation at 470 nm and emission at 590 nm. The protein concentration of exosome lysates was determined by DC protein assay (Bio-Rad Laboratories). Standards and samples (5 μL) were added into a 96-well plate, followed by addition of 25 μL reagent A:S at a ratio of 50:1, and 200 μL of reagent C. The absorbance at 750 nm was measured after 15 min incubation at room temperature. The concentration of exosome lysates was calculated based on a standard calibration curve. For western blotting analysis, the collected exosomes were lysed in RIPA buffer containing protease inhibitor (1X). After denaturing at 95 °C for 5 min, the lysate was resolved in SDS-PAGE gel and transferred onto nitrocellulose membrane, followed by incubation with primary antibody (1:1000 dilution) at 4 ºC overnight and secondary antibody

(1:5000 dilution) at room temperature for 1 h. The blot was imaged using enhanced chemiluminescence (ECL).

Small animal models. For imaging and therapy studies, a U87MG subcutaneous mouse model was used. The animal model was established by subcutaneously inoculating 1 million U87MG cells onto the right hind leg or the right flank (for PET imaging only) of a 5-6 week old athymic female nude mice (Harlan). For toxicity studies, normal 5-6 week old balb/c mice (Envigo laboratories). All the animal studied were performed according to a protocol approved by the Institutional Animal Care and Use Committee (IACUC) of University of Georgia.

***In vivo* MRI and Prussian blue staining.** Human serum albumin decorated iron oxide nanoparticles (HSA-IONPs) were prepared according to a previously published protocol[3]. HSA-IONPs (20 μg Fe mL^{-1}) and DSN-52 (20 μg Dox mL^{-1}) were co-incubated with RAW264.7 cells for 2 h for cell labeling. The resulting, IONP labeled cells at a dose of around 2 million cells per mouse were i.v. administrated to nude mice bearing U87MG tumors on the right hind leg (tumor size ≈ 200 mm^3). The mice were scanned on a 7.0 T Varian small animal MRI system before cell injection, as well as 1, 4 and 24 h after the administration. The scan parameters were the following: TR = 2500 ms, TE = 40 ms, field-of-view (FOV) = 40 mm × 80 mm, matrix size = 2562, thickness = 2 mm. After the 24-h scan, the mice were euthanized. The liver, spleen, lung, heart, kidney, brain, and tumor tissues were collected and frozen in optical cutting temperature (OCT) compound gel at -80 °C for Prussian Blue staining purpose. The tissue blocks were cryo-sectioned into 8 μm thick slices and fixed in formalin solutions for 10 min. The slides were carefully rinsed with PBS twice and then submerged in a solution containing 20% HCl and 10%

$K_4[Fe(CN)_6]\cdot 3H_2O$ for 20 min (Prussian Blue Staining). Afterwards, the slices were washed twice with PBS and counter-stained with Fast Red for 5 min, followed by PBS wash.

Small-animal Positron Emission Tomography. Small-animal PET was performed on a micro-PET R4 scanner. U87MG tumors were inoculated to the right flanks of the nude mice instead of their hind legs to minimize the impact from tracer uptake in the abdomen. Imaging started once the tumor size reached 50-100 mm^3. DSN-MF and MF cells were co-incubated with ^{64}Cu-pyruvaldehyde-bis(N4-methylthiosemicarbazone) (^{64}Cu-PTSM) in 1 mL serum-free medium at 37 ^{o}C for 1.5 hours. After washing, 1 million of ^{64}Cu-labelded cells in 0.25 mL PBS (pH 7.4) were i.v. injected into each mouse under isofluorane anesthesia. Static scans were performed at various time points (i.e., 1, 8, and 23 h after the injection). The average radioactivities accumulated within the tumor and other major organs were quantified from decay-corrected coronal images and the results were converted to percentage injected dose per gram (%ID g^{-1}).

***In vivo* therapy study.** Treatments started when tumor size reached 100~150 mm^3. 25 mice were randomly divided into 5 groups and were i.v. injected with PBS, free Dox, DSN-52 in PBS, MF cells, and DSN-MF cells on Day 0. Dox, DSN-52, and DSN-MF were injected at 3 mg Dox kg^{-1}, and 4 million cells were injected into the mice in MF and DSN-MF groups. The body weight and tumor volume of each mouse were measured every other day for 2 weeks. The tumor volume was calculated by the following equation: tumor volume = $0.5 \times \text{length} \times (\text{width})^2$, where length $\geq$ width. Mice were euthanized once the tumor volume was above 1,700 mm^3.

In separate studies, animals were euthanized 24 h after cell/drug injection, and the tumors were collected and frozen in OCT compound gel at -80 ^{o}C. The tissues were cryo-sectioned into 8 μm thick slices for *in situ* apoptosis detection staining (ab206386 from abcam) following the vendor's protocol. The apoptotic nuclei were stained as dark brown and the cytoplasm components were green.

Toxicity studies. Fifteen normal balb/c mice were randomly divided into 5 groups and received regimens specified in the *in vivo therapy study* section. The body weight and anal temperature of each mouse were measured daily at the same time (starting from 6 days before injection through Day 6). On Day 7, all mice were euthanized and the whole blood was collected. Part of the blood samples were used for a complete blood count (CBC) test. The rest were centrifuged at 5000 rcf for 5 min and the resulting serum samples were stored at -80 ^{o}C and then subjected to ELISA or colorimetric assays to quantify C-reactive protein (CRP), TNF-α, alanine transaminase (ALT), aspartate aminotransferase (AST), and blood urea nitrogen (BUN) amounts. All tests were conducted by following the vendors' protocols. CRP and TNF-α kits were purchased from RayBiotech, ALT (MAK055) and AST (MAK052) kits from Sigma-Aldrich, and BUN from Arbor Assays. Each assay was repeated at least twice.

Statistical methods. Quantitative data were expressed as mean ± SEM. Two-tailed Student's t-test and Chi-squared test were used for statistical comparison between experimental groups and control groups for different studies. $P < 0.05$ was considered statistically significant.

Estimation of drug loading capacity via surface backpack strategy

The number of cells injected during one transfer procedure is calculated to evaluate the drug loading capacity of nanoparticle-laden cell system via surface backpack strategy. Three types of nanoparticles that are commonly used for drug loading are considered here: (1) poly(lactic-co-glycolic acid) (PLGA) nanoparticle; (2) lipid-type nanoparticle, such as liposome; (3) Stöber silica nanoparticle. For each particle, three parameters are considered for the estimation: (a) the amount drug in each particle, (b) the number of nanoparticles that are tethered on surface of each cell, and (c) the injection dose. The following equation is used to estimate the drug loading amount per nanoparticle: drug loading by weight = %Loading Capacity × nanoparticle weight. Except some rare examples[4], the %Loading Capacity by weight of PLGA nanoparticle, lipid nanoparticle, and Stöber silica nanoparticle is typically lower than or close to 20%[5–8]. The nanoparticle weight can be calculated by mass = density × volume. The density of PLGA nanoparticle, lipid nanoparticle, and Stöber silica nanoparticle is around 1.3 g cm^{-3}, 1.06 g cm^{-3}, and 1.8-2.2 g cm^{-3} respectively. Assuming each nanoparticle is a perfect sphere, the volume of a single nanoparticle equals to $(4/3)\pi r^3$, where r is the radius of nanoparticles, typically ranging from 100 to 200 nm. According to Stephan et al.[9], attachment of up to 100-150 nanoparticles with a diameter of ~200 nm onto the plasma membrane is benign to T cells and hematopoietic stem cells. A clinically relevant treatment dose usually ranges from 1 to 10 mg kg^{-1}.

To simplify the calculation, we assume drug encapsulated nanoparticle as a homogeneous entity with a fixed density, the %Loading Capacity = 20%, and the number of nanoparticles attached onto each single cell = 300. At 1 mg kg^{-1}, which is at the low end of typical drug injection dose, and assuming a body weight of 25 g for mouse and 50 kg for human, the amount of drug injected is 25 μg per mouse and 50 mg per person. As shown in the following table, the drug loading capacity on a per cell basis is estimated around 0.03-0.50 pg drug $cell^{-1}$, which requires to inject tens to hundreds million cells per mouse to achieve the 1 mg kg^{-1} dose. In a recent report by

Huang et al. about using nanoparticle-carrying T cells for drug delivery[10], the drug loading was 0.1~0.125 pg drug cell^{-1}, which coincides well with our estimation.

Table S1. **Estimation of drug loading per cell via the surface backpack strategy**

NP type	**density**	**radius**	**volume**	**NP mass**	**drug / NP**	**drug / cell**	**#cell / mouse**	**#cell / person**
	g cm^{-3}	nm	cm^3	pg	pg NP^{-1}	pg cell^{-1}	million	billion
PLGA	1.30	50	0.52×10^{-15}	0.68×10^{-3}	1.36×10^{-4}	0.04	612	1224
		100	4.19×10^{-15}	5.45×10^{-3}	10.89×10^{-4}	0.33	77	153
Lipid	1.06	50	0.52×10^{-15}	0.56×10^{-3}	1.11×10^{-4}	0.03	751	1501
		100	4.19×10^{-15}	4.44×10^{-3}	8.88×10^{-4}	0.27	94	188
Stöber Si	2.00	50	0.52×10^{-15}	1.05×10^{-3}	2.09×10^{-4}	0.06	398	796
		100	4.19×10^{-15}	8.38×10^{-3}	16.76×10^{-4}	0.50	50	99

NP: nanoparticle

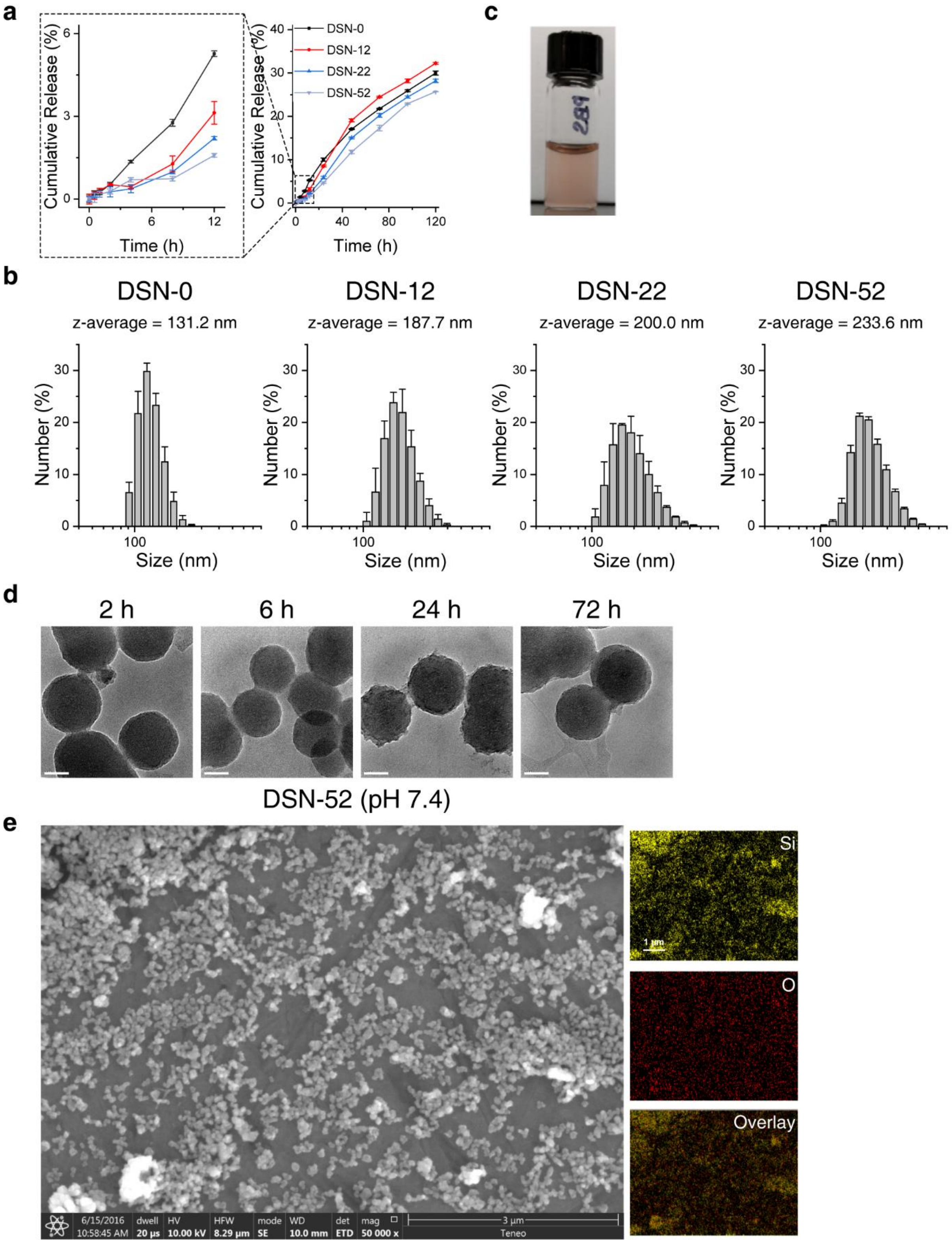
a
Cumulative Release (%)
0
3
6
0
6
12
Time (h)
Cumulative Release (%)
0
10
20
30
40
0
40
80
120
Time (h)
DSN-0
DSN-12
DSN-22
DSN-52
c
281
b
DSN-0
z-average = 131.2 nm
DSN-12
z-average = 187.7 nm
DSN-22
z-average = 200.0 nm
DSN-52
z-average = 233.6 nm
Number (%)
0
10
20
30
100
Size (nm)
d
2 h
6 h
24 h
72 h
DSN-52 (pH 7.4)
e
6/15/2016 10:58:45 AM
dwell 20 µs
HV 10.00 kV
HFW 8.29 µm
mode SE
WD 10.0 mm
det ETD
mag 50 000 x
3 µm
Teneo
Si
1 µm
O
Overlay

Figure S1. a) Drug release profiles at pH 7.4 and **b)** hydrodynamic sizes of DSN-0, DSN-12, DSN-22, and DSN-52 nanoparticles. **c)** Digital photograph of DSN-52 nanoparticle dispersed in PBS. **d)** TEM images showing DSN-52 nanoparticles' morphology changes over time in a pH 7.4 PBS solution. Scale bar, 50 nm. **e)** SEM and elemental mapping by EDS with DSN-52 nanoparticles.

Table S2. Loading capacity (%LC) of DSNs

	Total Wt. mg	**Dox** mg	**SiO_2** mg	**Dox Ratio** wt%
DSN-0	5.0	0.83	4.17	16.70%
DSN-12	2.6	0.29	2.39	11.15%
DSN-22	4.7	0.42	8.34	8.94%
DSN-52	6.7	0.34	6.36	5.13%

Table S3. Loading capacity (%LC) of DSN-52 by ICP-OES.

	Dox μg	**Si** ppm	**Soln.** g	**Si** ppm	**Si** μg	**SiO2** μg	**Total** μg	**Dox Ratio** wt%
BKG	0	0.97	5.03	0	0	0	0	
#1	6	10.51	(5mL)	9.54	47.986	102.8271	108.8271	5.51%
#2	12	22.4		21.43	107.793	230.985	242.985	4.94%

average	5.23%

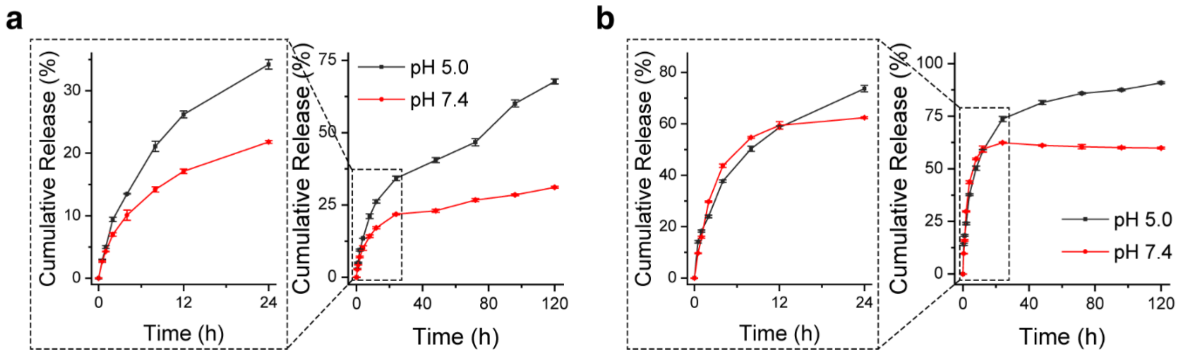

Figure S2. Drug release profiles measured at pH 5.0 and 7.4 with **a)** Doxove and **b)** Dox-encapsulated mesoporous silica nanoparticles.

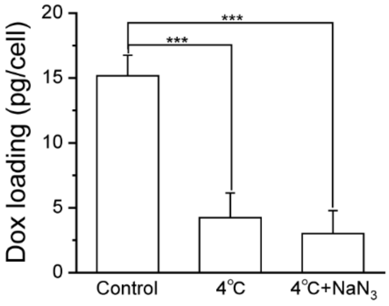

Figure S3. Drug loading assay showing the internalization of DSN-52 nanoparticles into macrophage. Control, DSN-52 nanoparticles were laden into RAW264.7 cells via incubation under normal condition; 4°C, loading was conducted at 4°C; 4°C+NaN_3, loading was conducted at 4°C with the presence of 0.1 wt.% NaN_3. ***, $p<0.001$.

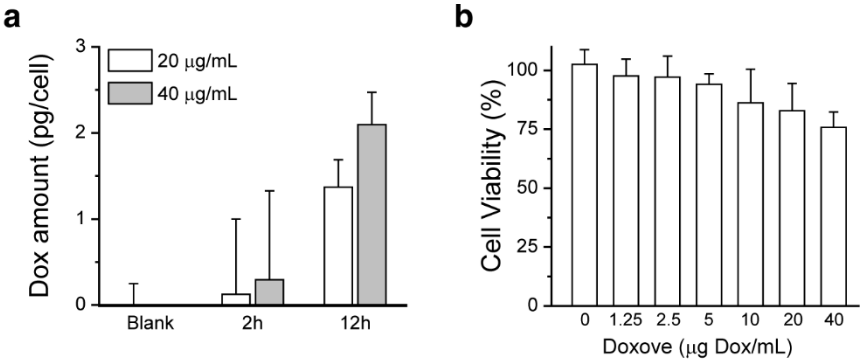

Figure S4. a) Intracellular Dox contents. RAW264.7 cells were incubated with Doxove at 20 and 40 μg Dox/mL for 2 or 12 h. **b)** Cell viability. RAW264.7 cells were incubated with Doxove at different concentrations for 2 h. After replenished with fresh media, the cells were cultured for 24 h, and the viability measured by MTT.

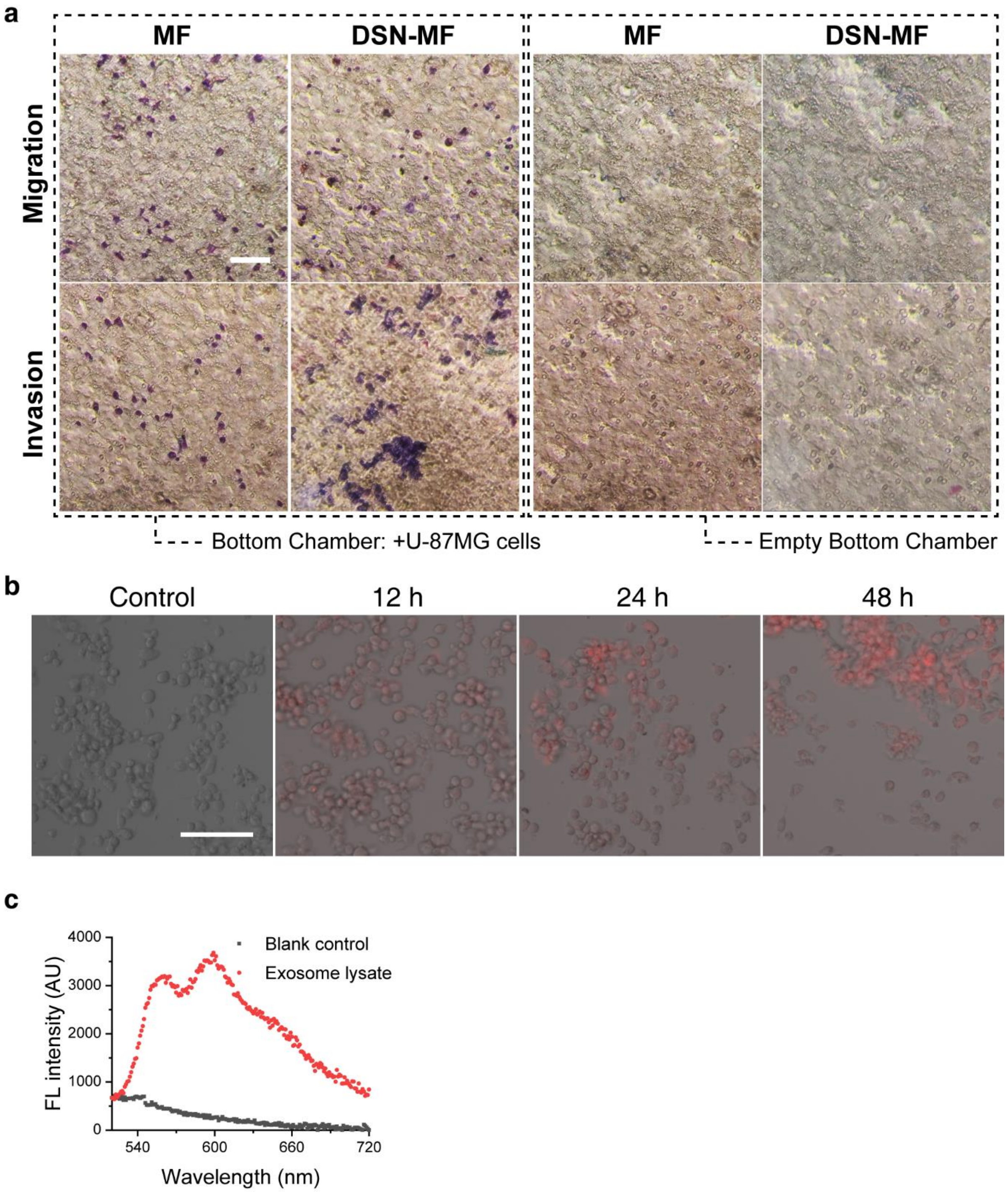

Figure S5. a) Transwell invasion/migration assay results. **b)** FL images of U87MG cells after incubating with different supernatants from DSN-MF cell cultures for 6 h. **c)** FL spectroscopy analysis of exosome lysates, which confirms the presence of Dox in the exosomes. Excitation was set at 470 nm.

Table S4. Dox release from DSN-MF

# cells (× 10^6**)**	**Dox$_{load}$** (μg)	**Dox$_{exo}$** (μg)	**Dox$_{sup}$** (μg)	**%Dox release**	**%Dox(exosome)**
5.03 ± 0.13	80.03 ± 2.00	7.51 ± 0.47	37.93 ± 1.07	56.8%	16.5%

- %Dox release = $(\text{Dox}_{exo} + \text{Dox}_{sup})/\text{Dox}_{load} \times 100\%$
- %Dox(exosome) = $\text{Dox}_{exo}/(\text{Dox}_{exo} + \text{Dox}_{sup}) \times 100\%$

Dox$_{load}$: the amount of Dox loaded in 5.03 ± 0.13 × 10^6 RAW264.7 cells; **Dox$_{exo}$**: the amount of Dox in secreted exosomes; **Dox$_{sup}$**: the amount of Dox present in the supernatant.

Note: a certain amount of Dox is retained in the cell debris, which was removed during centrifugation and excluded from calculation.

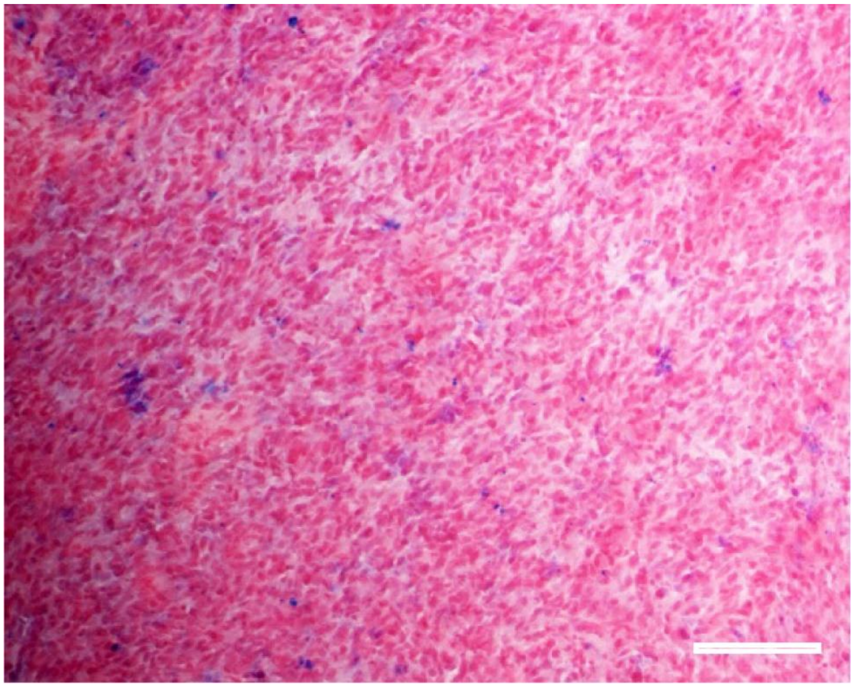

Figure S6. Prussian blue staining on tumor cryo-section. Tumors were collected at 24 h after i.v. injection with IONP-labeled DSN-MF cells.

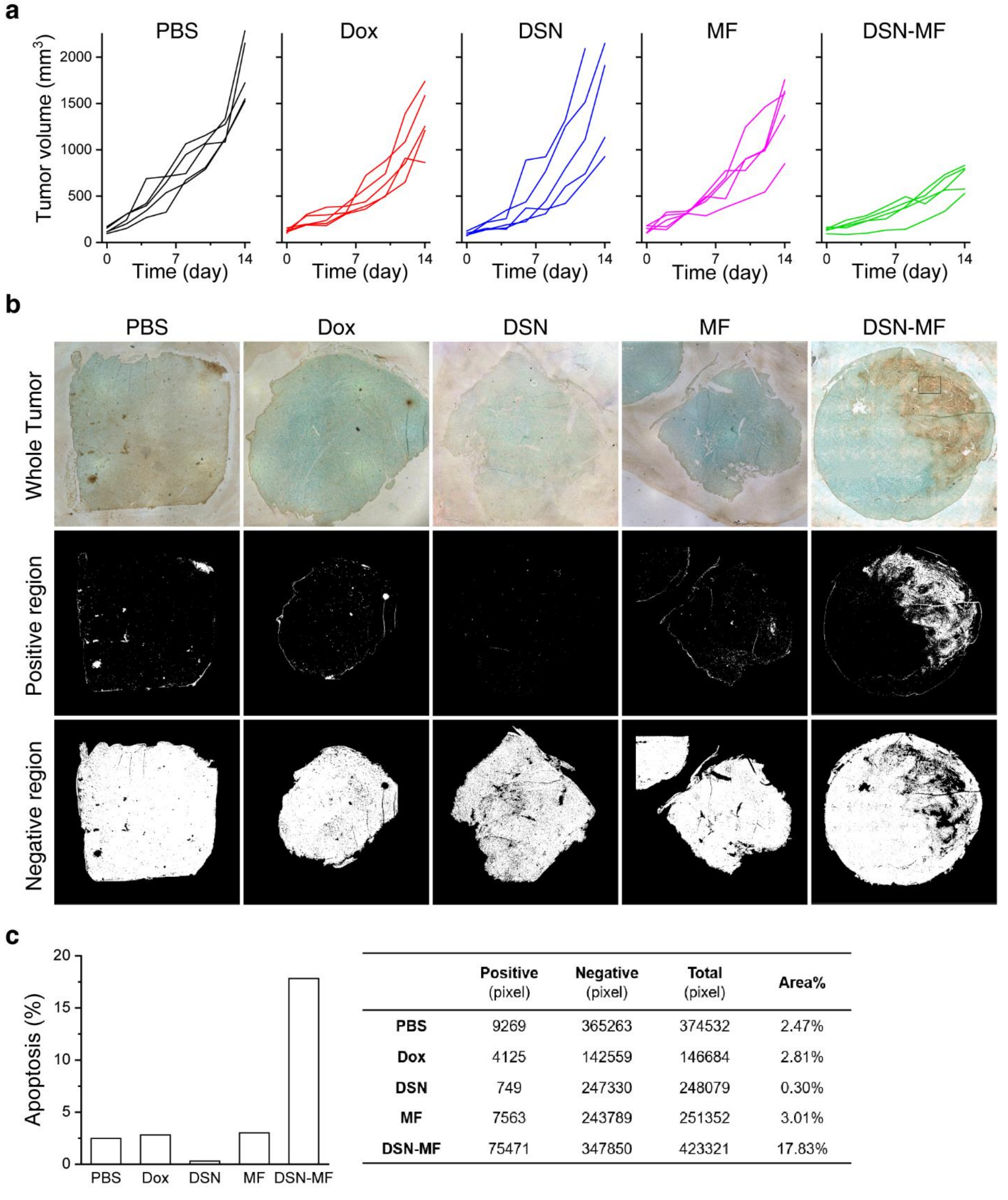

	Positive (pixel)	Negative (pixel)	Total (pixel)	Area%
PBS	9269	365263	374532	2.47%
Dox	4125	142559	146684	2.81%
DSN	749	247330	248079	0.30%
MF	7563	243789	251352	3.01%
DSN-MF	75471	347850	423321	17.83%

Figure S7. a) Tumor growth curves for individual animals. **b)** *In situ* Apoptosis staining analysis of cryo-sectioned tumor tissues. The tumors were dissected 24 h post treatments. The whole tumors were subjected to staining and the positively stained areas quantified by Photoshop. **c)** Quantitative analysis based on the staining results of **b**.

Table S5. Complete Blood Count Report

	PBS	**Dox**	**DSN**	**MF**	**DSN-MF**	**REF. RANGE**
WBC ($\times10^3$ µl^{-1})	5.62	13.49	6.31	3.77	8.52	6-15
RBC ($\times10^6$ µl^{-1})	9.26	13.9	9.34	8.81	8.39	7-11
HGB (g dl^{-1})	14.0	44.0	14.1	13.7	13.1	1.2-16.6
HCT (%)	44.7	48.9	44.4	43.4	41.4	39-49
MCV (fl)	48.3	15.4	47.6	49.2	49.4	41-49
MCH (pg)	15.1	31.6	15.1	15.5	15.6	15-18
MCHC (g dl^{-1})	31.3	62	31.8	31.6	31.7	30-38
Segs (%)	10	0	13	13	13	10-40
Bands (%)	0	12	0	0	0	No data
Lymphs (%)	84	82	79	80	78	55-95
Monos (%)	6	6	8	7	9	1-4

REFERENCE

[1] S. Zhang, Z. Chu, C. Yin, C. Zhang, G. Lin, Q. Li, *J. Am. Chem. Soc.* **2013**, *135*, 5709.

[2] W. X. Mai, H. Meng, *Integr. Biol. (United Kingdom)* **2013**, *5*, 19.

[3] J. Xie, J. Wang, G. Niu, J. Huang, K. Chen, X. Li, X. Chen, *Chem. Commun. (Camb).* **2010**, *46*, 433.

[4] J. Della Rocca, R. C. Huxford, E. Comstock-Duggan, W. Lin, *Angew. Chemie - Int. Ed.* **2011**, *50*, 10330.

[5] P. Kan, C.-W. Tsao, A.-J. Wang, W.-C. Su, H.-F. Liang, *J. Drug Deliv.* **2011**, *2011*, 1.

[6] D. J. A. Crommelin, L. van Bloois, *Int. J. Pharm.* **1983**, *17*, 135.

[7] X. Song, Y. Zhao, S. Hou, F. Xu, R. Zhao, J. He, Z. Cai, Y. Li, Q. Chen, *Eur. J. Pharm. Biopharm.* **2008**, *69*, 445.

[8] M. García-Díaz, C. Foged, H. M. Nielsen, *Int. J. Pharm.* **2015**, *482*, 84.

[9] M. T. Stephan, J. J. Moon, S. H. Um, A. Bershteyn, D. J. Irvine, *Nat. Med.* **2010**, *16*, 1035.

[10] B. Huang, W. D. Abraham, Y. Zheng, S. C. Bustamante López, S. S. Luo, D. J. Irvine, *Sci. Transl. Med.* **2015**, *7*, 291ra94.